

1 Southern limit of the Patagonian Ice Sheet

2

3 Dominic A Hodgson¹, Stephen J Roberts¹, Eñaut Izagirre², Bianca B Perren¹, François De
4 Vleeschouwer³, Sarah J. Davies⁴, Thomas Bishop⁵, Robert D McCulloch^{6,7}, Juan-Carlos Aravena^{8,9}

5

6 1 British Antarctic Survey, High Cross, Madingley Road, Cambridge, CB3 0ET, UK

7 2 Department of Geography, Prehistory and Archaeology, University of the Basque Country

8 UPV/EHU, Vitoria-Gasteiz, Spain

9 3 Instituto Franco-Argentino para el Estudio del Clima y sus Impactos, (CNRS-IRD-CONICET-UBA),

10 Dpto. de Ciencias de la Atmosfera y los Oceanos, FCEN, Universidad de Buenos Aires, Argentina

11 4 Geography and Earth Sciences, Llandinam Building, Penglais Campus, Aberystwyth University, SY23

12 3DB

13 5 Department of Geography, Arthur Lewis Building, Oxford Road, Manchester M13 9PL

14 6 Centro de Investigación en Ecosistemas de la Patagonia, Coyhaique, Aysén, Chile

15 7 School of GeoSciences, The University of Edinburgh, Edinburgh, EH8 9XP

16 8 Centro de Investigación Gaia Antártica, Universidad de Magallanes, Punta Arenas, Chile

17 9 Cape Horn International Center (CHIC), Puerto Williams 6350000, Chile

18

19 Corresponding author: Dominic A Hodgson. Email daho@bas.ac.uk

20

21

22 **Abstract**

23 The southern latitudinal limit of the Patagonian Ice Sheet at the Last Glacial Maximum is poorly
24 constrained due to a paucity of field data. This particularly applies to southern outlet glaciers of the
25 Cordillera Darwin Ice Field whose full extents have been debated by glacial geologists since 1899 CE,
26 impacting estimates of total ice volume. Here we report on the stratigraphy of exposed stratigraphic
27 sections on the west coast of Isla Hermite which include glacial tills overlain by successions of peats
28 and sandy silt. The location and orientation of the tills suggest that an ice lobe extended south from
29 Cordillera Darwin across an extended Magellan outwash plain through Paso Mantellero and past
30 Islas Hermite and Cabo de Hornos (Cape Horn). This was similar in extent to the Canal Beagle and
31 Lago Fagnano Ice Lobes which extended to the east. Maximum extent occurred sometime before
32 12,880 cal. yr BP based on radiocarbon dated peat macrofossils. We discuss whether this is a close
33 minimum age, or a product of delayed onset of peat accumulation at the sampling site. We provide a
34 brief interpretation of the Late Glacial and Holocene palaeoenvironmental history of the island from

35 deposits overlying the till, and from peat cores inland. These suggest peatland initiation before
36 15,400 cal. yr BP and the establishment of woody Magellanic moorland peat from 12,880 cal. yr BP
37 possibly indicating a southward shift of the SHW during the early Holocene climate optimum.

38

39 **Key Words**

40 Quaternary, Glaciation, South America, Patagonia, Geomorphology, glacial

41

42

43 **1. Introduction**

44

45 The changing extent of the Patagonian Ice Sheet at glacial maxima has been extensively mapped
46 from moraines, trimlines, drift deposits and other terrestrial and offshore glacial geomorphology.
47 This data, accumulated over more than 180 years, has been refined with increasing methodological
48 and chronological rigour as new techniques become available. Notable advances include the
49 systematic descriptions of geomorphological deposits, the widespread application of radiocarbon
50 and other isotope dating methods to constrain the age of glacial features, and time slice
51 reconstructions of whole ice sheet glaciation (see Davies et al., 2020 and references therein).

52

53 Despite these advances, there are still extensive regions where former Last Glacial Maximum (LGM)
54 ice sheet extents remain poorly constrained, or where the geomorphological evidence is not reliably
55 characterised or dated. These have been identified in recent empirical reconstructions of the ice
56 sheet. Regions identified by Davies et al. (2020) include the ‘eastern Chilean Lake District, most
57 outlet lobes in the Isla Grande de Chiloé sector, southcentral and western Patagonia through the
58 archipelago and numerous outlet lobes of the Southern Patagonian Ice Field’. This is important
59 because past changes in regional glacier mass provide a basis for the validation models projecting
60 future glacier responses to climate (Dussaillant et al., 2019). Currently ice loss from the Southern
61 Andes approximates 18.7 Gt yr⁻¹ accounting for c. 7% of global glacier mass change 2000–2019 CE
62 (Hugonet et al., 2021) linked with decadal changes in precipitation and temperature.

63

64 At the southern limits of the Patagonian Ice Sheet, reconstructions of the former ice margins
65 associated with the Cordillera Darwin Ice Field (54.5°S, Fig. 1B) have been inferred with ‘low
66 confidence’ (Fig. 33 in Davies et al., 2020). This is because many of the ice lobes terminated offshore,
67 are in difficult areas to access and study on land or have not been reliably characterised or dated.
68 There are notable exceptions around the Estrecho de Magallanes, Bahía Inútil (Bentley et al., 2005;

69 Darvill et al., 2015; Peltier et al., 2021) and Canal Beagle ice lobes (Coronato et al., 2004) where
70 observational data underpins ‘high’ to ‘medium confidence’, and ‘medium confidence’ assessments
71 respectively (Fig. 35 in Davies et al., 2020). Otherwise, most estimates of LGM and earlier limits in
72 these areas rely on models (Hulton et al., 2002), and inferences of former glacial troughs from low
73 resolution bathymetry, often on the basis of little direct evidence. As a result, there is a long history
74 of conflicting interpretations of maximum ice extents in this region. These range from inferred LGM
75 ice extents at or near the edge of the continental shelf in the earliest reconstructions by
76 Nordenskjöld (1899), to LGM limits on the southern shore of Isla Navarino and eastern shore of Isla
77 Hoste (Caldenius, 1932). These, and more recent interpretations are reviewed in Rabassa et al.,
78 (2011).

79

80 The southernmost lobe of the Cordillera Darwin Ice Field, inferred to extend south of Isla Navarino,
81 through Bahia Nassau towards the Islas Wollaston, Islas Hermite and Cabo de Hornos (Cape Horn)
82 remains particularly poorly constrained (Fig. 2A). Recent whole ice sheet GIS based landform
83 assessments and GEBCO bathymetry infer the presence of a glacial trough with ‘low confidence’,
84 extending from the Cordillera Darwin, around Peninsula Dumas and Peninsula Hardy on Isla Hoste,
85 towards the continental shelf break at 55-56°S (Davies et al., 2020). However, there is no direct
86 evidence of an ice stream occupying this region apart from inferences of ice extending south-south
87 east across Isla Hoste (Coronato et al., 1999). In this paper, we describe glacial deposits, and peat
88 and shallow lake sediment records from the west coast of Isla Hermite that suggest an LGM ice lobe
89 extended along Paso Mantellero, between Isla Hoste and Isla Hermite towards the edge of the
90 continental shelf at 56°S (Fig. 2A). This marks the southern limit of the LGM Patagonian Ice Sheet.

91

92 1.1 Site description

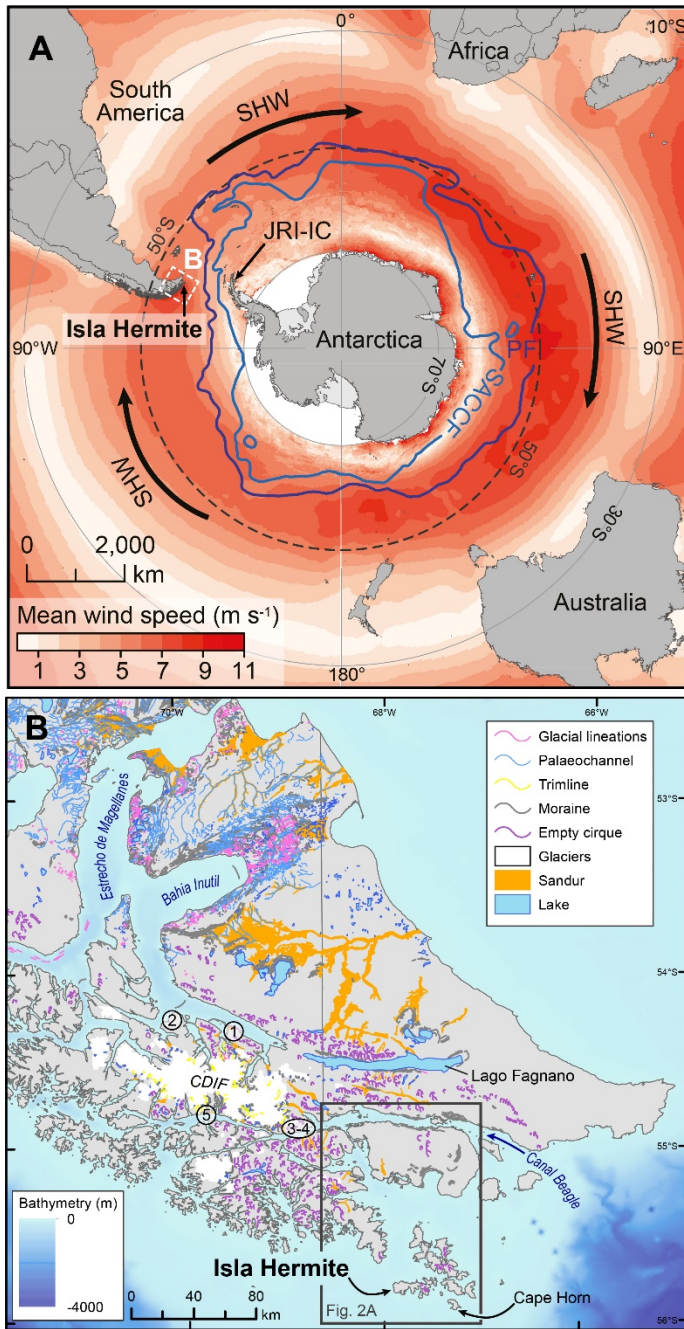
93 Isla Hermite (55°51'S, 67°40'W, Fig 2) is the westernmost of the Islas Hermite, which include Isla
94 Hornos and Cabo de Hornos. Isla Hermite is named after Jacques L'Hermite, who led the “Nassau
95 Fleet,” around Cape Horn in 1624; its native Yaghan name is Samajani. The island is located at the
96 southernmost limit of the South American continent, 100 km south of Puerto Williams (Isla
97 Navarino) and within the Cabo de Hornos National Park. It has a sub polar oceanic climate
98 dominated by the Southern Hemisphere westerly winds (SHW, Fig 1A), which have a local mean
99 monthly intensity of 18.59 to 22.72 knots (34 to 42 km h⁻¹) and a maximum of 123 knots (228 km h⁻¹).
100 Temperatures range from -1 to 13°C, and the monthly mean relative humidities range from 85 to
101 89.6 % (data from 40 km east of the sampling site at Cabo de Hornos Lighthouse; Centro
102 Meteorológico Marítimo de Punta Arenas). The geology of the island comprises the Jurassic-

103 Cenozoic intrusives and volcanic rocks characteristic of the south-western side of the Fuegian Andes
104 (Torres Carbonell et al., 2016). The geomorphology of the eastern part of the island consists of
105 rounded hills rising to c. 516 m, while the western part of the island has generally lower relief (30-
106 100 m, reaching a maximum altitude of 427 m at Cerro West) (Fig. 2B). The vegetation consists of
107 Magellanic moorland including cushion plants, grasses, lichens and mosses, with extensive peat bogs
108 and shallow peatland ponds at lower altitudes. Fragments of dwarf shrub heathland and stunted
109 Magellanic subpolar forest trees including *Nothofagus antarctica* and *N. betuloides* persist inland
110 and in protected valleys. Hill summits are largely devoid of higher vegetation but retain lichens and
111 mosses (Fig. 2B).

112

113 There are no published direct observations on the glacial geomorphology of Isla Hermite. Analysis of
114 remotely sensed images has inferred five empty glacial cirques on the eastern (higher) parts of the
115 island (shown on Fig. 2A), and some potential glacial lineations oriented NNW to ESE were inferred
116 from linear features on a promontory on the north east coast (Glasser and Jansson, 2008). The latter
117 have not been ground-truthed or included in later compilations of the regional glacial
118 geomorphology (Davies et al., 2020).

119



120
121
122 Figure 1. A. Location of Isla Hermite within the core belt of the Southern Hemisphere Westerly
123 Winds (SHW) and north of the Southern Antarctic Circumpolar Current Front (SACCF) and Polar Front
124 (PF). B. Subset of PATICE (Davies et al., 2020) showing a regional overview of the glacial
125 geomorphological features derived from former Cordillera Darwin outlet glaciers. Locations cited in
126 the text: 1 Punta Marinelli; 2 Punta Esperanza; 3 Caleta Olla; 4 Ventisquero Holanda; 5 Bahía Pía. The
127 black box outlines the region South of Canal Beagle shown in Fig. 2.

128 **2. Methods**

129

130 We carried out a geomorphological survey to identify evidence of glaciation on Isla Hermite, within a
131 day's walk of a camp established on the north coast. This included examining areas of bare rock for
132 glacial striations, looking for landforms associated with glacial transport including erratic boulders,
133 examining stratigraphic sections exposed by wind, fluvial or wave erosion, and sampling and
134 describing the stratigraphy of sediment cores from peat bogs, peat depressions with surface water,
135 and shallow ponds.

136

137 Stratigraphic sections were examined at sites within and adjacent to coastal cliffs at Cabo West (SS2,
138 55.8438°S, 67.9091°W, ~30–45 m GPS altitude) and Punta Momberg (SS1, 55.8295°S, 67.8991°W,
139 ~14–20 m GPS altitude) (Fig. 3A). Characterisation of the section at Cabo West included visual
140 description of lower units exposed in the inaccessible cliff face at 55.8432°S, 67.9104 °W, direct
141 sampling of mid units exposed by coastal erosion, and sampling of upper units by coring through an
142 overlying raised peat dome (HER42PB at 55.8433°S, 67.9095°W) and an adjacent peat depression
143 with 20 cm surface water (HER42L at 55.8433°S, 67.9095°W) (Fig. 4A). Core sampling of other nearby
144 peat depressions and shallow ponds was carried out to determine the spatial extent of the
145 stratigraphic units identified in the coastal section (Fig. 4A and C: HER44L at 55.8442°S, 67.9072°W,
146 0.2 m deep; and HER49L at 55.8515°S, 67.9025°W, 0.5 m deep). Characterisation of the section at
147 Punta Momberg included direct sampling of units exposed by coastal erosion and coring of the
148 overlying peat (Fig. 4A and B). A basic clast fabric analysis was carried out on the lowest unit by
149 measuring the compass orientation of the long axes of elongate clasts. Core sampling of other
150 nearby peat depressions and shallow ponds was also carried out (Fig. 4A and B: HER 14L at
151 55.8264°S, 67.8911°W, 0.4 m deep; HER24L at 55.8289°S, 67.8949°W, 0.5 m deep; HER34L at
152 55.8351°S, 67.9097°W, 0.5 m deep).

153

154 Stratigraphic sections were cleaned to reveal the succession of facies, photographed and selected
155 layers subsampled. Peat bogs, peat depressions with surface water and shallow ponds were sampled
156 on foot (peat cores) or from a tethered boat (pond cores). Cores were retrieved using a 'Russian'
157 peat corer (Belokopytov and Beresnevich, 1955) in 50 cm sections, from adjacent holes (20 cm
158 apart), with a 10 cm overlap between each core section. A Glew mini corer was used to collect the
159 upper flocculent surface sediments in the ponds. Core sections were described, photographed, and
160 transferred into 50 cm PVC half-pipe in the field, wrapped in cling film and layflat tubing, kept cool
161 during transport to the UK, and then frozen and vacuum-packed for storage.

162

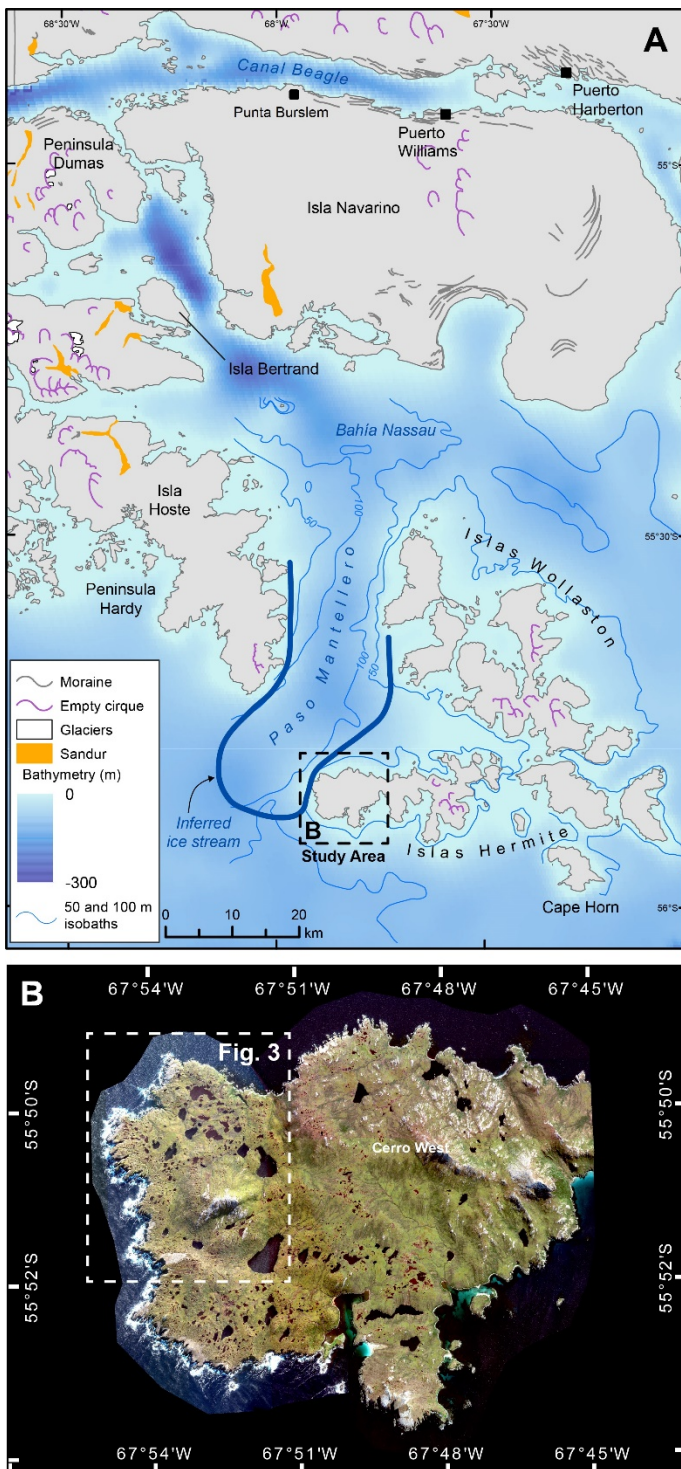
163 Cores were defrosted slowly while vacuum-packed to minimise shrinkage and examined to provide a
164 basic description of the sedimentary facies. Non-destructive Geotek® multi-sensor core logging
165 (MSCL) (Gunn and Best, 1998) was undertaken for gamma-ray wet density (γ -density; GRD),
166 resistivity, magnetic susceptibility (MSk; $S\text{lx}10^{-5}$; Bartington Instruments: MS2E point sensor, 2 or 5
167 mm interval; 10 seconds measurement time) and volume specific (density-corrected) $\text{MS}\chi$ (κ/ρ ; kg m^{-3})
168 data, processed using Geotek Software (Gunn and Best, 1998).

169

170 Digital X-radiographs were obtained using the ITRAX® X-ray fluorescence core scanner at
171 Aberystwyth University (settings: 45 kV, 50 mA, 200 ms, 60 μm or 200 μm measurement interval).
172 Contiguous and non-destructive downcore Energy Dispersive Spectrometry (EDS) X-ray fluorescence
173 core scanning (XRF-CS) was then undertaken using the same core scanner and a Molybdenum (Mo)
174 anode X-ray tube (settings: 30 kV, 50 mA, count time 10 seconds per 1 mm distance travelled by the
175 detector). XRF-CS calibration and performance checks were undertaken using a synthetic glass
176 standard and XRF fused glass discs from Ardley and Yanou Lake sediment cores in the South
177 Shetland Islands (Roberts et al., 2017). Spectral data were processed in Q-spec v8.6.0 (Cox
178 Analytical) to optimise model fit and produce element peak-area calculations. MSE values were
179 minimised to produce optimal fit between ‘as measured’ spectra and modelled spectra. Data were
180 processed using itrax.R (Bishop, 2021), filtering out individual outlier spectra with low total cps
181 (defined as less than mean total cps minus 4 std. dev, mainly due to gaps in the cores), and
182 exceptionally elevated MSE values (defined as greater than mean MSE plus 4 std. dev, representing a
183 poor fit between measured to modelled spectra) and elevated core surface slope values. Here, we
184 focus on incoherent (Compton; henceforth, inc.) and coherent (Rayleigh; henceforth coh.) scatter
185 data ratios as established proxies for changes in water (and organic) content (inc./coh.; Davies et al.,
186 2015) and dry mass (coh./inc.; Boyle et al., 2015) and $\ln(\text{K}/\text{Ca})$ ratios as proxies for changing
187 mineralogenic inputs. Since Ca has multiple potential sources (principally: erosion, aerosol and dust
188 input, carbonates), normalisation of K by Ca is used to highlight: 1) increased erosion of K-rich
189 feldspars, which are commonly found in clays and fine dust, and reflect >erosion and >wind
190 transport; 2) deposition of exotic dust and aerosols that are richer in K than local wind-blown or
191 eroded material; 3) far-travelled rhyolitic tephra produced by explosive eruptions from the Andean
192 Cordillera characterised by significantly elevated K compared to Ca (e.g. McCulloch et al., 2020;
193 Smith et al., 2019; Stern et al., 2016)

194

195 Core sections were aligned into composite records from field depth measurements, visual
196 stratigraphy, digital X-radiographs, bulk density, MS, XRF-CS scan data.
197
198 To provide chronological constraints, plant macrofossils from the top, bottom and main transitions
199 within the stratigraphic sections, sediment and peat cores were radiocarbon dated. Sediments and
200 soils were acid washed; macrofossils had acid/alkali/acid pre-treatment. Radiocarbon analyses were
201 performed at various labs (Beta Analytic USA, Keck-CCAMS Group USA, Scottish Universities
202 Environmental Research Centre, Laboratoire de Mesures du Carbone 14 in Paris). Calibration of
203 radiocarbon ages was undertaken in OxCal v.4.4 (Bronk Ramsey, 2016) using the SHCal20.14C
204 Southern Hemisphere atmosphere calibration dataset (Hogg et al., 2020). Radiocarbon ages are
205 reported as conventional radiocarbon years BP (^{14}C years BP) $\pm 1\sigma$ and calibrated ages as 2σ (95.4%)
206 ranges, median and mean calendar years BP (cal a BP and cal ka BP, relative to 1950 CE), rounded to
207 the nearest ten years. Bayesian age-depth models were constructed using BACON v.2.5 (Blaauw and
208 Christen, 2011).



209

210

211 Figure 2. A. Subset of PATICE (Davies et al., 2020) showing an overview of the terrestrial glacial
 212 geomorphology the region South of Canal Beagle together with bathymetry derived from GEBCO
 213 data and representations of isobaths from hydrographic charts (Armada-de-Chile, 2000). Blue line
 214 shows the location of the inferred 'Paso Mantellero Ice Stream', Red box shows the Isla Hermite
 215 study area in B. B. Western part of Isla Hermite including Punta Momberg and Cabo West. White box
 216 shows the location of the lower panel. Image from Digital Globe WorldView-2, acquired 28th April
 217 2012.

218

219

220 **3. Results**
221
222 3.1 Glacial geomorphology
223 Evidence of glacial geomorphology was limited in the study area, except for basal units in the
224 stratigraphic sections at Cabo West and Punta Momberg, described below. Three rock surfaces were
225 found on upland areas which had linear erosion features (Supplementary Fig. 1), but with different
226 orientations. All displaced boulders were derived from local bedrock outcrops rather than other
227 Tierra del Fuego geologies. Inland peat exposures typically showed the accumulation of peat directly
228 on bedrock or boulder-strewn bedrock surfaces (Supplementary Fig. 2) with maximum depths of
229 peat exceeding 4 m.

230
231 3.2 Stratigraphic sections
232 The west coast of Isla Hermite consists of a series of small headlands, deeply incised inlets and
233 coastal blowouts extending up to 500 m inland, formed by direct exposure to Southern Ocean swells
234 and the Southern Hemisphere Westerly Winds (SHW) (Fig. 3A). Along parts of this coastline, erosion
235 of the cliffs has exposed a sequence of late Quaternary deposits not observed immediately inland of
236 the cliffs or elsewhere in the study area. The sequence was exposed at two sites: Cabo West (Figs.
237 3A and 4), and Punta Momberg (Figs. 3A and 5). It consists of four main Stratigraphic Units spread
238 over a depth of ~10–14 m at Cabo West, and ~ 2–4 m at Punta Momberg.

239
240 Unit I, the basal unit, is in contact with the bedrock. It is a poorly sorted diamicton (Dmm) consisting
241 of subangular to rounded boulders up to ~ 70 cm in length embedded within a sandy silty-clay
242 matrix. Unit I is ~ 2–3 m deep and exposed in the cliff face at Cabo West (Fig. 4D) and immediately
243 inland of the cliff at Punta Momberg (Fig 5C). Analysis of clast orientations in Unit I at Punta
244 Momberg showed the long axes of most clasts were orientated between 330–0° (Fig. 6).

245
246 At both sites, there is a sharp contact between Units I and II. Unit II consists of a dark brown
247 desiccated peat with intact roots and woody fragments. Five radiocarbon dates were used to date
248 this contact. Macofossil radiocarbon ages on plant fragments immediately below and above the
249 contact at Punta Momberg (Fig. 5B) had median calibrated ages of 12880 and 12740 cal. yr BP (Fig.
250 7A, Table 1). Bulk sediment ages were younger at 7760 and 10320 cal. yr BP respectively, which we
251 attribute to leaching of the humic acid fraction from the exposed face of the overlying peat (where it
252 is subject to oxidation and high rainfall). At Cabo West the Units I to Unit II transition could not be

253 directly sampled for dating due to its inaccessible location in the cliff face, but the age of the deepest
254 accessible Unit II peat was 10,640 cal. yr BP (Fig. 7C, D, Table1).

255

256 Unit III consists of layered grey-brown sands and silts. This 102 cm thick unit was deposited over a
257 relatively short period of 640 years from 8650 – 8010 cal. yr BP at Cabo West (Fig. 4C). An
258 equivalent, but much thinner 3 cm layer was deposited around 8234 cal. yr BP at Punta Momberg
259 (Fig. 5B).

260

261 Unit IV consists of a relatively uniform Holocene peat with sand and grit layers, occasional clasts and
262 fibrous plant remains. This was deposited from 8010 cal. yr BP at Cabo West (Fig. 4A–C), and from
263 sometime after 8230 cal. yr BP at Punta Momberg (Fig. 5A, B). At Cabo West the radiocarbon dating
264 shows that the lower part of the Unit IV peat core (HER42PB) overlaps with the Unit IV peat sampled
265 in the exposure showing that the full sequence was sampled (Fig. 7A). The peat core (HER42PB) and
266 adjacent peat depression (HER42L) both sample the Unit IV peat and have similar composition and
267 accumulation rates (0.089 and 0.075 cm yr⁻¹ from the surface to 339 cm and 276 cm depths,
268 respectively) (Fig. 7A).

269

270 3.3 Sediment cores

271 Sediment cores from the shallow peat depressions and ponds in the vicinity of Cabo West (HER44,
272 0.15 km southeast of the stratigraphic section (SS2) and 0.05 km inland; HER49L, 0.85 km south
273 southeast and 0.1 km inland) had median basal ages of 8780 and 8800 cal. yr BP (Figs. 3C and 7E,
274 Table 1). Both consisted of sediments with density and density corrected magnetic susceptibility
275 values contiguous with the Unit IV peats. There is no evidence of the lower Units I–III sampled at
276 Cabo West (Fig. 4) in the magnetic susceptibility or in the erosion/dust aerosol (Ln K/Ca) data (Fig
277 3C). Therefore, we assume the Unit IV peats at these locations accumulated on bedrock.

278

279 Sediment cores from the shallow near-coastal peat depressions and lakes in the vicinity of Punta
280 Momberg (HER14L, 0.55 km northeast of the Punta Momberg stratigraphic section (SS1) and 0.32
281 km inland; HER24L, 0.2 km east and 0.2 km inland; and HER34, 1 km southwest and 0.11 km inland)
282 have median basal ages of 15,400, 9290 and 4300 cal. yr BP respectively (Figs. 3B, 7C and D, Table 1).
283 Both consisted of sediments with density and density corrected magnetic susceptibility values
284 contiguous with the Unit IV peats (Fig. 3B). There is no evidence of the lower Units I–III sampled at
285 and prior to 8230 cal. yr BP in the coastal Punta Momberg stratigraphic section in the magnetic

286 susceptibility or erosion/dust aerosol (Ln K/Ca) data (Fig 3B). These peats have similar properties to
287 Unit IV and therefore we assume they also accumulated on bedrock.

288

289 HER14L is a shallow pond (0.4m deep) with a sediment record accumulating from 15,400 cal. yr BP
290 (Figs. 3B and 7C). There was a hiatus in sediment accumulation after 10,650 cal. yr BP, and evidence
291 of Holocene reworking in the top 75 cm of the record, where most ages are < c. 2000 cal a BP (Fig.
292 7C, Table 1). We attribute the loss of the early and mid- late-Holocene parts of this record to wind
293 mixing causing remobilisation and deflation, noting the large coastal blowout that currently extends
294 to within 30 m of the lake shore (Fig. 3A). These coastal blowouts can also erode into and capture
295 the lakes, as seen elsewhere on the island (e.g., 55.8305°S, 67.8661°W). Collectively, the sediment
296 cores in the vicinity of Punta Momberg show near continuous peat deposition on this part of the
297 island since the Late Glacial from a minimum age of 15,400 cal. yr BP (Figs. 3B and 7C) (except for a
298 1540-year gap between the beginning of the hiatus in HER14 at 10,650 cal. yr BP and onset of peat
299 deposition in HER24 at 9110 cal. yr BP).

300

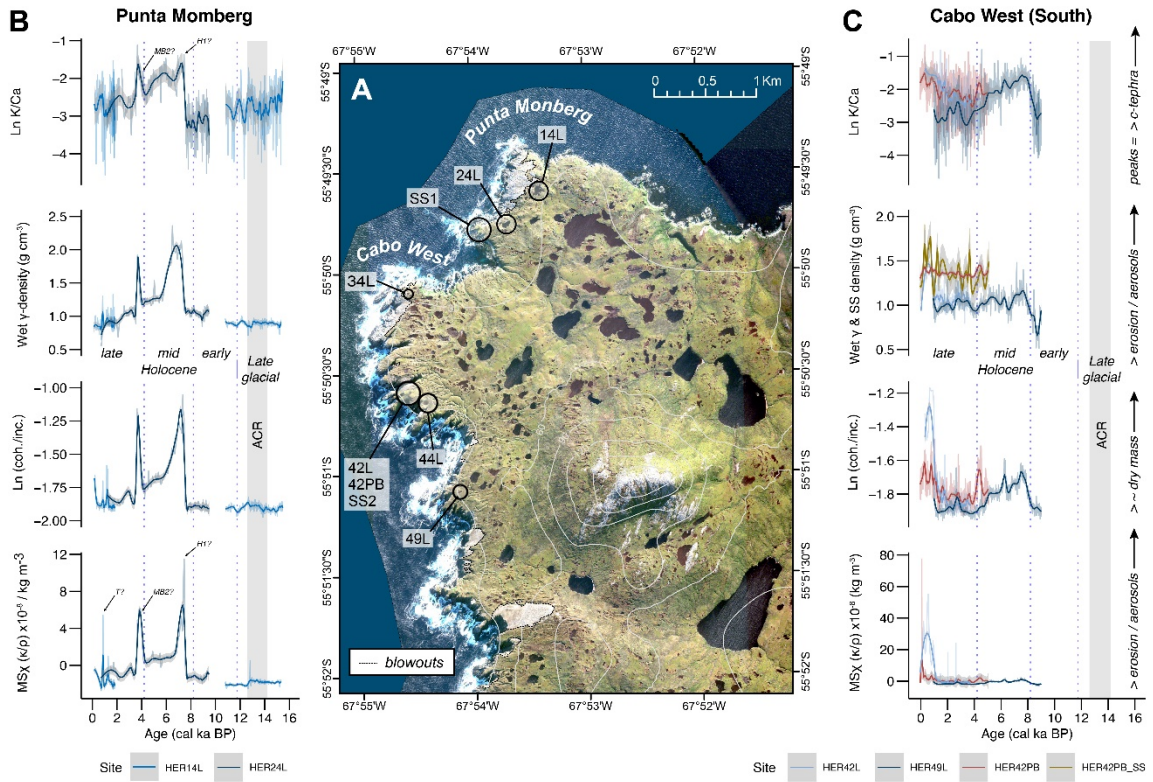
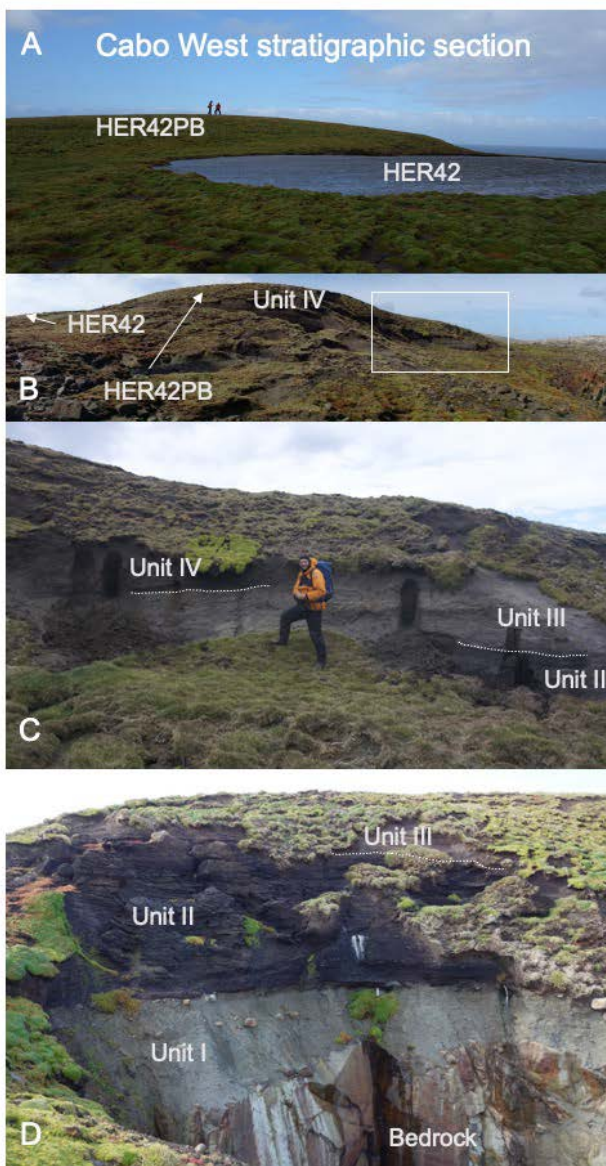


Figure 3

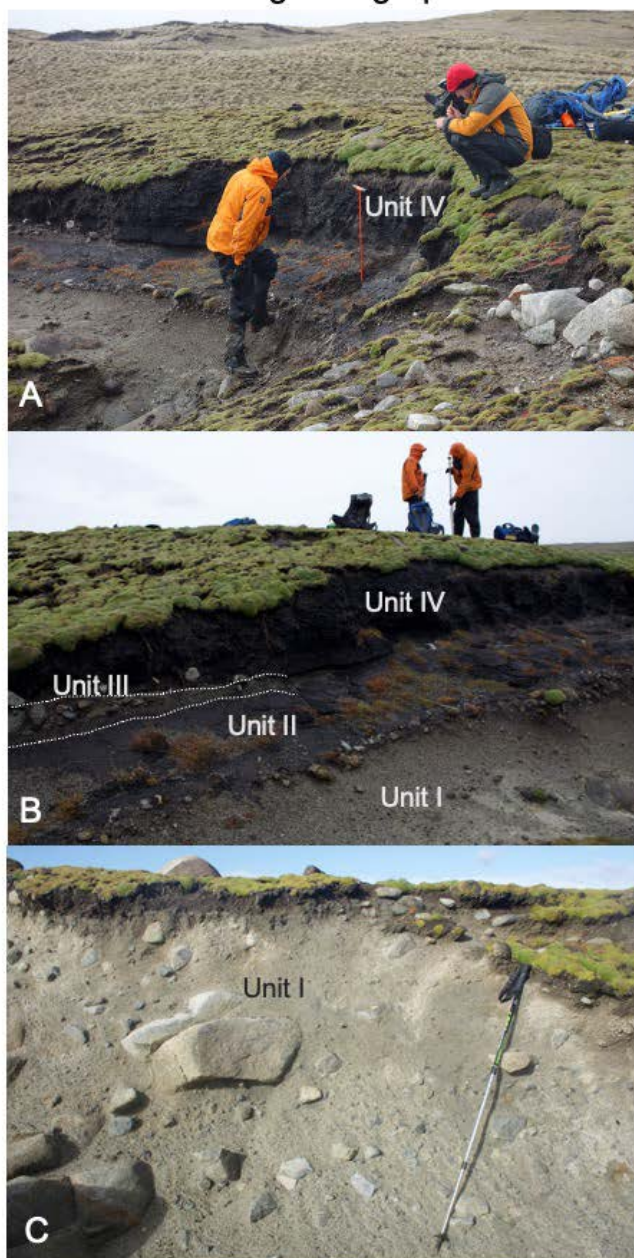
301
302 Figure 3. A Detail of the west coast of Isla Hermite showing locations of the stratigraphic sections
303 sampled at Punta Momberg (SS1) and Cabo West (SS2), peat cores (HER42PB), and numbered
304 shallow lake cores (HER14L, 24L, 34L, 42L, 44L, and 49L). Dotted lines mark the locations of extensive
305 coastal blowouts. Image from Digital Globe WorldView-2, acquired 28th April 2012. B. Summary data
306 for lake sediment and peat records from the Punta Mombeg area. C. Summary data for lake
307 sediment and peat records from the Cabo West area. These include proxies for organic/minerogenic
308 shifts including density corrected magnetic susceptibility (MS_X) dry mass (coh./inc.), wet density and
309 Ln(K/Ca) ratios.



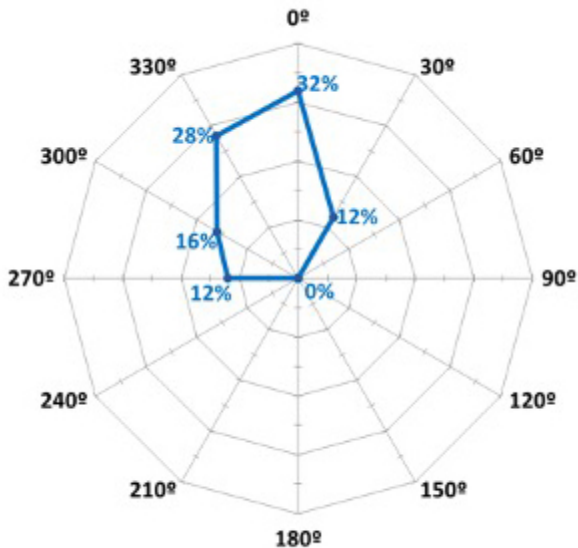
310
311

312 Figure 4. Cabo West stratigraphic section (location SS2 in Fig. 3) showing photographs of the four
313 lithological units from which samples were collected: Unit I Poorly sorted bouldery diamicton, Unit II
314 woody peat, Unit III sands and clays, Unit IV Holocene peat. A. Top of the section showing the
315 domed peat bog (HER42PB) and the shallow pond (HER42L) from which sediment cores were
316 extracted to sample the upper parts of Unit IV. B. View of the deposits from the west coast showing
317 the location of the exposed part of the section. C. detail of the exposed section from which the lower
318 parts of Unit IV, Unit III and the upper parts of Unit II were sampled. D. The base of the section as
319 seen in the adjacent c. 70 m cliff face showing the underlying bedrock and Units I–III. This base of
320 Unit II was inaccessible without rope access, so samples for radiocarbon dating the Unit I – Unit II
321 transition were collected at the Punta Momberg stratigraphic section.
322
323
324

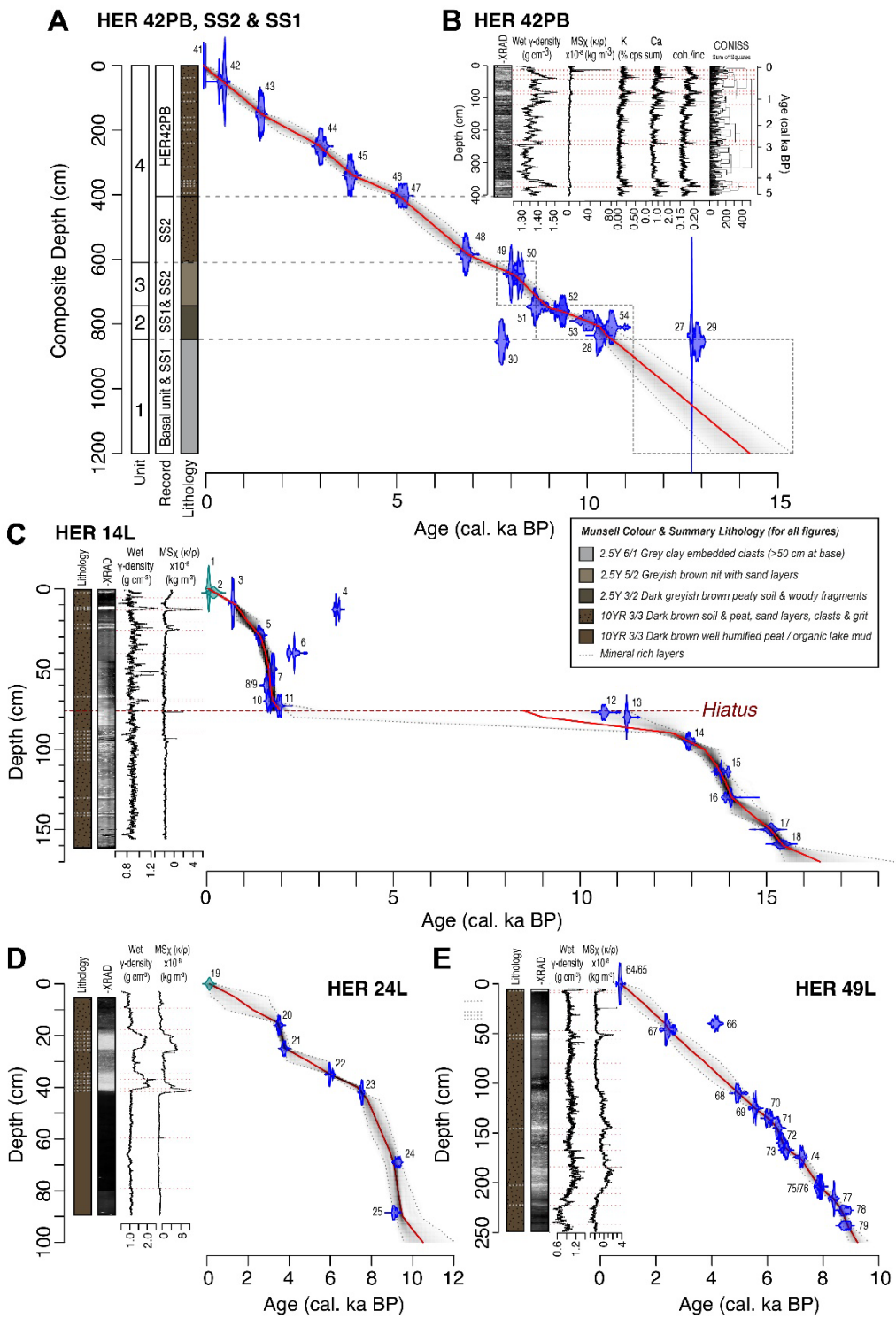
Punta Momberg stratigraphic section



328 Figure 5. Punta Momberg stratigraphic section (location SS1 on Fig. 3) showing photographs of the
329 four lithological units from which samples were collected. A. Overview of the section. B. Detail
330 showing Units I-IV. C. Detail showing Unit I with a walking pole for scale.



332
333 Figure 6. Rose plot showing clast orientation in the Unit I in the Punta Momberg stratigraphic section
334 (SS1). The majority of clasts were orientated between 330-0°, suggesting deposition by N-S trending
335 ice.



336
337

338 Figure 7. A. Composite age depth model of the Cabo West Stratigraphic Section consisting of data
339 from SS2 and the overlying HER42PB (Fig 3) with ages for the base of Unit II dated by samples from
340 Punta Momberg (SS1; Fig. 5). B. X-ray image and selected XRF-CS measurements from the HER42PB
341 peat core, which captures the upper 5160 cal. yr BP of Unit I in the Cabo West stratigraphic section.
342 C. Age depth model and selected MSCL measurements for HER14L. D. Age-depth model and selected
343 MSCL measurements HER24L. E. Age-depth model and selected MSCL measurements for HER49L.
344 Radiocarbon age probability distributions indicated by numbers relate to ID numbers shown in Table
345 1; MSCL data is plotted in Supplementary Figures S4-S7.

ID	Record N-S	Lab ID	Sample ID	Depth [Strat.dept h] cm		Sample type	$\delta^{13}\text{C}_{\text{VPD}}$		^{14}C Abs.		Radiocar bon Age		Calibrated age (cal a BP) [SHCal20; 2-sigma, 95.4]				Notes	
				B %	C %		(wt. %)	modern	Enrichment SD	^{14}C SD	max.	min.	Mean	SD	Median			
				h	cm													
1	HER14L	UCIAMS-1763	HER14-2A-0	0		organic sediment	-26.4	34.3	98.62	0.17	50	##	60	20	50	20	50	RES
2	HER14L	SUERC-70108	HER14-2A-02.5	2.5		wood	-24.7	31.0	96.69	0.45	207	##	300	-	180	80	190	
3	HER14L	UCIAMS-1763	HER14-2A-09	9		organic sediment	-27.5	27.8	89.73	0.23	805	##	730	660	700	20	700	
4	HER14L	UCIAMS-1763	HER14-2A-13	13		organic sediment	-27.9	25.7	65.71	0.13	3310	##	3570	3400	3490	40	3480	REV
5	HER14L	SUERC-70109	HER14-2A-29	29		wood	-26.9	32.0	81.56	0.38	1574	##	1530	1310	1420	50	1420	
6	HER14L	UCIAMS-1763	HER14-2A-40	40		peat	-27.9	27.1	73.84	0.14	2370	##	2460	2150	2310	80	2340	
7	HER14L	UCIAMS-1763	HER14-2B-10	50		peat	-28.1	29.1	78.54	0.14	1875	##	1830	1700	1770	30	1780	
8	HER14L	BETA-515202	HER14-2B-20	60		peat	-28.6	-	74.54	0.28	2360	##	2430	2150	2280	90	2320	REV
9	HER14L	BETA-512780	HER14-2B-20	60		plant material	-28.3	-	80.42	0.30	1750	##	1700	1530	1620	50	1620	
10	HER14L	BETA-512781	HER14-2B-30	70		peat	-26.7	-	79.73	0.30	1820	##	1820	1590	1680	50	1690	
11	HER14L	BETA-572833	HER14-2B-33	73		Plant material	-28.4	-	77.77	0.29	2020	##	2010	1830	1940	40	1930	H
12	HER14L	BETA-572834	HER14-2B-37	77		Plant material	-26.1	-	30.80	0.12	9460	##	10760	10510	10650	70	10650	
13	HER14L	UCIAMS-1763	HER14-2B-40	80		macrophytic peat	-27.8	31.7	28.90	0.09	9905	##	11320	11200	11250	30	11250	
14	HER14L	UCIAMS-1764	HER14-2C-15	95		macrophytic peat	-25.1	25.0	25.13	0.08	11030	##	13070	12780	12920	60	12910	
15	HER14L	UCIAMS-1764	HER14-2C-34	114		macrophytic peat	-28.9	33.1	22.37	0.08	11965	##	14020	13600	13820	100	13790	
16	HER14L	UCIAMS-1764	HER14-2D-20	130		macrophytic peat	-28.2	38.4	21.84	0.09	12160	##	14110	13810	13990	80	14030	
17	HER14L	UCIAMS-1764	HER14-2D-40	150		macrophytic peat	-25.4	31.9	20.38	0.08	12715	##	15260	14970	15120	70	15120	
18	HER14L	BETA-429318	HER14-2D-49	159		peat	-21.8	-	20.02	0.10	12920	##	15600	15220	15410	100	15400	
19	HER24L	SUERC-70116	HER24-3A-0	0		plant material	-27.2	46.1	97.39	0.45	148	##	280	-	120	80	110	RES
20	HER24L	SUERC-70117	HER24-3A-16	16		peaty sediment	-26.3	42.3	65.63	0.30	3319	##	3590	3390	3500	50	3500	
21	HER24L	SUERC-70118	HER24-3A-25	25		organic sediment	-28.3	6.8	64.04	0.30	3516	##	3880	3630	3750	60	3760	
22	HER24L	UCIAMS-1822	HER24-3B-05*	35		organic sediment	-28.9	5.9	51.61	0.17	5250	##	6180	5900	5990	70	5970	
23	HER24L	SUERC-70119	HER24-3B-12*	42		organic sediment	-28.0	21.1	43.14	0.20	6689	##	7590	7430	7520	40	7530	
24	HER24L	SUERC-70123	HER24-3B-39	69		peat	-27.4	53.2	35.21	0.17	8321	##	9440	9030	9280	90	9290	
25	HER24L	BETA-429317	HER24-3C-49	88.5		peat	-24.6	-	36.03	0.20	8200	##	9280	9000	9120	80	9110	
26	PMSS	BETA-617952	XRF6_125	115		sandy soil	-23.5	-	39.66	0.15	7430	##	8350	8030	8220	80	8230	
27	PMSS	BETA-617951	XRF6_95_m	145 [835]		plant material	-24.4	-	26.04	0.10	10810	##	12760	12700	12740	10	12740	
28	PMSS	BETA-617849	XRF6_95_sed	145 [835]		organic sediment	-26.0	-	31.85	0.16	9190	##	10490	10230	10330	70	10320	REV
29	PMSS	BETA-617950	XRF6_75_m	165 [855]		plant material	-24.4	-	25.40	0.13	11010	##	13070	12770	12890	70	12880	
30	PMSS	BETA-617848	XRF6_75_sed	165 [855]		organic sediment	-25.8	-	41.99	0.16	6970	##	7920	7670	7760	50	7760	REV
31	HER34L	UCIAMS-1764	HER34-1A-0	10		plant material	-28.1	-32.2	96.93	0.17	185	##	280	-	180	80	210	
32	HER34L	UCIAMS-1764	HER34-1A-40	50		peat	-28.2	-33.7	68.97	0.13	2920	##	3150	2880	3020	60	3010	
33	HER34L	BETA-429315	HER34-2A-48	58		organic sediment	-26.9		61.46	0.23	3910	##	4420	4150	4300	70	4300	
34	HER42L	UCIAMS-1764	HER421A-0	0		peaty sediment	-17.0	-24.8	99.52	0.17	39	##	60	20	40	20	40	
35	HER42L	UCIAMS-1764	HER421A-07	7		mossy peat	-26.4	-26.9	86.13	0.20	1135	##	1060	930	1000	40	990	
36	HER42L	UCIAMS-1764	HER421B-34	70		peat	-26.3	-28.4	79.51	0.14	1780	##	1710	1580	1650	30	1650	
37	HER42L	UCIAMS-1764	HER421C-14	90		peat	-26.8	-27.0	77.60	0.14	1975	##	1930	1830	1880	30	1880	
38	HER42L	UCIAMS-1764	HER421D-40	156		peat	-26.9	-26.0	71.96	0.13	2580	##	2750	2490	2630	80	2630	
39	HER42L	UCIAMS-1764	HER421E-35	191		peat	-26.3	-28.9	70.07	0.13	2795	##	2940	2770	2850	40	2850	
40	HER42L	BETA-429321	HER421G-49	276		peat	-25.6	-	65.00	0.24	3460	##	3830	3570	3690	70	3670	
41	HER42PB	ARTEMIS-6224	HER42PB-1A	0		peat macrofossil	-27.1	-	102.87	0.25	-227	##	-64	-67	-66	2	-66	PB
42	HER42PB	ARTEMIS-6224	HER42PB-1B	50.4		peat macrofossil	-26.8	-	94.39	0.48	465	##	540	320	460	60	480	
43	HER42PB	ARTEMIS-6224	HER42PB-1D	150		peat macrofossil	-23.9	-	81.99	0.23	1595	##	1530	1370	1450	50	1450	
44	HER42PB	ARTEMIS-6224	HER42PB-1G	250.3		peat macrofossil	-24.3	-	69.50	0.22	2920	##	3160	2880	3020	70	3010	
45	HER42PB	ARTEMIS-6224	HER42PB-1I	339.7		peat macrofossil	-25.9	-	64.20	0.22	3560	##	3910	3690	3800	60	3790	
46	HER42PB	BETA-478308	HERPB421J-48	403		peat	-27.3	-	56.97	0.21	4520	##	5310	4970	5150	90	5160	
47	HER42SS	SUERC-64000	HER42SS_405	405		peat	-27.0	35.30	58.07	0.27	* 4367	##	5040	4830	4920	60	4910	
48	HER42SS	BETA-429320	HER42SS_225	585		peat	-25.6	-	-	-	6020	##	6950	6680	6820	60	6820	
49	HER42SS	SUERC-63996	HER42SS_165	645		peat	-27.6	24.70	40.57	0.20	* 7246	##	8170	7930	8030	60	8010	
50	HER42SS	SUERC-63995	HER42SS_63	747		peat	-28.1	4.84	37.43	0.18	* 7894	##	8980	8540	8680	100	8650	
51	HER42SS	SUERC-63994	HER42SS_50R	760		root	-25.3	50.30	35.38	0.17	* 8347	##	9460	9130	9320	90	9330	
52	HER42SS	SUERC-63993	HER42SS_50	760		peat	-27.7	39.50	35.32	0.17	* 8361	##	9470	9140	9330	80	9350	
53	HER42SS	SUERC-63992	HER42SS_20	790		peat	-27.9	52.70	32.95	0.16	* 8917	##	10190	9770	10000	110	10010	
54	HER42SS	SUERC-63991	HER42SS_80	810		peat	-28.4	58.9	30.82	0.16	* 9454	##	10990	10500	10650	80	10640	
55	HER44L	SUERC-68864	HER44-2A-0	0		plant and sediment	-26.8	8.9	92.17	0.40	591	##	630	500	560	40	550	RES
56	HER44L	SUERC-68865	HER44-2A-09	9		peaty sediment	-18.0	8.6	93.65	0.43	463	##	540	320	460	60	480	
57	HER44L	SUERC-68866	HER44-2A-16	16		peaty sediment	-28.1	1.0	52.91	0.23	5050	##	5900	5600	5760	80	5750	
58	HER44L	SUERC-68867	HER44-2B-11	22		and-peaty sediment	-28.3	0.5	36.64	0.17	8001	##	9000	8640	8830	100	8830	
59	HER44L	SUERC-68871	HER44-2B-22	33		organic sediment	-28.0	3.2	36.41	0.18	8053	##	9020	8650	8870	90	8870	
60	HER44L	SUERC-70123	HER44-2B-34A	43		wood	-26.4	31.0	38.02	0.18	7705	##	8550	8380	8460	50	8460	
61	HER44L	SUERC-70124	HER44-2B-34B	43		peat	-28.0	6.4	34.39	0.17	8511	##	9540	9420	9490	40	9490	
62	HER44L	BETA-429316	HER44-2B-47	56		wood	-26.9	-	37.08	0.14	7970	##	8990	8600	8790	110	8780	
63	HER49L	SUERC-70125	HER491A-0	0														

347

348 Table 1.

349 Radiocarbon dates of stratigraphic sections, peat cores and lake sediment cores from Isla Hermite.
350 Calibration were carried out using OXCAL v. 4.4 using the SHCal20 Southern Hemisphere atmosphere
351 calibration dataset (Hogg et al., 2020). Calibrated ages have two-sigma (2σ ; 95.4%) maximum and
352 minimum age ranges and one-sigma (1σ ; 68%) error for the mean. To reflect dating and age-depth
353 modelling uncertainties, calibrated ages have been rounded to the nearest 10 calendar years (cal yr
354 BP). *C-14 enrichment; REV=reversal; RES=reservoir age; PB=post-bomb; H=hiatus.

355

356 **4. Discussion**

357

358 **4.1 Absence of whole island glaciation**

359 The absence of drift deposits and glacial geomorphology across the island suggests it was not
360 overridden during the last glaciation. If glacier ice was present, it likely only occupied the five
361 inferred glacial cirques on the eastern uplands previously described from satellite images (Glasser
362 and Jansson, 2008; but not confirmed by ground-truthing) and in the 25 ka time slice of the PATICE
363 reconstruction (Fig. 33 in Davies et al., 2020). A lack of consistency in the orientation of linear
364 features observed on local bedrock surfaces suggests these are not glacial striations, but erosion of
365 pre-existing weaknesses in the rock (Supplementary Fig. 1). The absence of geologically distinct
366 boulders, for example from the Lower Cretaceous plutonic and Devonian-Carboniferous
367 metamorphic rock that characterise the Cordillera Darwin (Sandoval and De Pascale, 2020), suggests
368 there was no long-range transport of erratics. The rounded nature of the hills could be the result of
369 earlier glacial activity but are more likely a product of intense salt and wind erosion; our
370 measurements of specific conductivity in 57 surface water samples from lakes on the west of the
371 island ranged from 0.3 to 7.1 mS cm⁻¹ (Salinity 0.1 to 3.9 PSU) resulting from sea salt aerosol
372 transport by winds which frequently reach gale force (28–55 knots). The dominance of the winds, in
373 combination with the low altitudes, would both have worked against in situ ice accumulation.

374

375 **4.2 Cordillera Darwin Ice lobe occupying Paso Mantellero (before 12,880 cal. yr BP)**

376 We interpret the deposition of glacial tills in the coastal sections at Cabo West and Punta Momberg,
377 as consistent with presence of an ice stream originating from Cordillera Darwin occupying Paso
378 Mantellero during the Last Glacial (before 12,880 cal. yr BP). The orientation of the clasts in Unit 1 is
379 indicative of a north to south ice flow direction rather than radial deposition by a local island ice cap
380 (Fig. 6), or a coalesced ice cap across the Islas Hermite; which would likely have been a single
381 landmass during period of lower (glacial) relative sea level (Björck et al., 2021; Guilderson et al.,
382 2000). A Last Glacial ice advance in Paso Mantellero has been inferred from PATICE LGM flowlines
383 (low confidence) (Davies et al., 2020), and 16 out of 21 gLGM PMIP model experiments with climate
384 forcing (Fig. 13 in Yan et al., 2022).

385

386 Paso Mantellero is a North-South trending submarine trough situated between Isla Hoste, Islas
387 Wollaston and Islas Hermite (Fig. 2A, Supplementary Fig. 3). The trough reaches depths of ~155 m
388 below present sea level, so much of it would have been subaerially exposed as part of the extended
389 Magellan outwash plain during glacial periods (Coronato et al., 1999), when relative sea levels have

390 been modelled between -45 to -115 m at 20 ka (Björck et al., 2021; Guilderson et al., 2000,
391 respectively). It has a broad valley landform characteristic of Patagonian land-terminating glacial
392 land systems formed by ice advances during periods of lower (glacial) sea levels (Davies et al., 2020).
393 GEBCO bathymetry captures the broad-scale morphology of the trough (Fig. 2A) with much finer
394 detail available in navigation charts which cannot be reproduced here (Armada-de-Chile, 2000). The
395 altitude of the base of Unit I in the Cabo West and Punta Momberg sections above the deepest part
396 of the trough provides a minimum constraint on ice lobe thickness of ~185–200 m.

397

398 The timing of the Paso Mantellero ice advance and retreat requires some consideration, as there is
399 evidence both for and against 12,880 cal. yr BP being a close minimum age for the Unit I to Unit II
400 transition. This is discussed below.

401

402 4.2.1 ‘Late Glacial advance hypothesis’

403 The accumulation of peat at HER14L shows that conditions for peat accumulation were established
404 on the island from at least 15,400 cal. yr BP (Her14, Figs. 3B and 7C), with peat accumulation
405 commencing above the Unit I glacial tills at Cabo West and Punta Momberg from 12,880 cal. yr BP.
406 The presence of the HER14L peat shows that there was a local source of plant propagules less than
407 550 m from the Punta Momberg stratigraphic section, potentially allowing for a relatively rapid
408 establishment of peat-forming plant communities on the glacial tills following ice retreat. This ‘Late
409 Glacial advance hypothesis’ requires the contiguous proximity of the glacier ice with fully vegetated
410 trough flanks, as observed in many Patagonian Glaciers today (e.g. Glacier Grey, Perito Moreno
411 Glacier).

412

413 Supporting evidence for Late Glacial ice advances in Patagonia include the ‘Magellan Late Glacial
414 advance’ at ‘15.3–12.2 ka’ which coincided with the Antarctic Cold Reversal (Sugden et al., 2005) and
415 cooler sea surface temperatures off the west coast of Chile at 41°S (Lamy et al., 2004). This coincides
416 with glacier recession and deglaciation in the Torres del Paine region after ‘12.5 ka’ (^{10}Be and ^{14}C
417 ages), from a maximum Antarctic Cold Reversal extent (the TDP II moraines) at ‘14.2 ± 0.5 ka’ (mean
418 ^{10}Be age) (García et al., 2012). Evidence for advanced positions, or retreat from advanced ice
419 positions, is also seen in some (but not all) of the Cordillera Darwin ice lobes around this time. For
420 example, there is evidence of ice dammed lakes in the central Estrecho de Magallanes ‘c. 17,000–
421 12,250 cal. yr BP’ (McCulloch et al., 2005a; Fig. 1B) with the last major advance of ice lobes into the
422 southern Estrecho de Magallanes dated between ‘c. 15,507–14,348 and 12,587–11,773 cal. yr BP’
423 (McCulloch et al., 2005b). At the Lago Fagnano ice lobe (Fig. 1B), onset of peat deposition from ‘TSP

424 San Pablo 1' east of Lago Fagnano commenced after '13,830–14,400' cal. yr BP, and after '12,710–
425 12,900 cal. yr BP' at 'LF Lago Fagnano' on the south east shore of the lake (Coronato et al., 2009).
426 The C4 moraine was then formed by a grounded ice terminus located towards the western end of
427 the lake at '11,170 cal. yr BP'; inferred from sedimentation rates below the H1 tephra dated at '7570
428 ± 120 cal. yr BP' (Waldmann et al., 2010) - the age of the H1 tephra was subsequently revised by
429 Stern et al. (2016) to 7891–8,440 cal yr. BP, based on radiocarbon dating of peat cores and lake
430 sediments respectively. The glacier advances at Lago Fagnano during this Late Glacial period have
431 been linked to enhanced precipitation, which started '≈14,200 cal. yr BP and persisted until ≈11,700
432 cal. yr BP' and promoted glacial growth and/or stabilization in the region, postponing their final
433 retreat into the early Holocene (Waldmann et al., 2010).

434

435 If the 'Late Glacial advance hypothesis' is correct, retreat of the Paso Mantellero Ice Lobe may have
436 been driven by postglacial relative sea level rise, which flooded the Magellan outwash plain,
437 converting the land terminating Paso Mantellero Ice Lobe into a marine terminating glacier. This
438 would have decreased the basal effective pressure of the ice lobe increasing the calving rate and
439 retreat of the calving front. Relative sea level reconstructions from nearby Canal Beagle, 110 km to
440 the north (Fig. 2A), show that relative sea level exceeded present day sea level from c. 11.5 ka,
441 reaching its maximum by c. 7 ka (Björck et al., 2021) so we can assume flotation of the glacier
442 terminus accelerated the retreat in the early Holocene. This interaction with relative sea level may,
443 in part, explain differences between glacier responses in marine terminating ice lobes in the
444 Magellan region compared with land terminating ice lobes of the Patagonian Ice Sheet at lower
445 latitudes.

446

447 4.2.2 'Early retreat hypothesis'

448 In contrast with the 'Late Glacial advance hypothesis', a number of models and geochronological
449 constraints suggest an earlier retreat of outlet glaciers from the Cordillera Darwin. For example, the
450 modelled ice advance in Paso Mantellero inferred from PATICE LGM flowlines occurred at about 35–
451 30 ka (low confidence) (Davies et al., 2020), and within the gLGM time slice in PMIP model
452 experiments (Yan et al., 2022; Fig. 13). The PATICE reconstruction shows that retreat of Cordillera
453 Darwin from its LGM extent commenced before 25 ka, reaching a configuration where major
454 Cordillera Darwin ice lobes terminated in Lago Fagnano, Canal Beagle and Isla Bertrand (Fig. 2A)
455 (medium confidence) and on Isla Hoste (Fig. 2A)(low confidence) by 20 ka (see Fig. 34 in Davies et al.,
456 2020).

457

458 Geochronological data from the northern ice lobes of Cordillera Darwin that discharge into Seno
459 Almirantazgo (Fig. 1B) and East into Canal Beagle also suggest an earlier retreat history, with no
460 evidence of a readvance during the Late Glacial. For example, minimum ages from peat bogs suggest
461 the eastern and central sectors of the Canal Beagle were ice free sometime before at '17,760 cal yr
462 BP' (Puerto Harberton, Fig. 2A) and '17,040 cal yr BP' (Punta Burslem, Fig. 2A) (McCulloch et al.,
463 2020), with the Puerto Harberton subsequently recording dust peaks from deglaciated forelands in
464 Canal Beagle during the Antarctic Cold Reversal and 'Younger Dryas' (Vanneste et al., 2015). At the
465 southern end of the Fuegan Andes directly north of Ushuaia and Canal Beagle, surface exposure ages
466 (¹⁰Be) from glaciated bedrock indicate that alpine areas were 'free of ice by ca 16.9 ka' with
467 subsequent ice advances limited to very local cirque glacier expansion (c. 2km) at '14.83' – '12.85 ka'
468 (¹⁰Be and ¹⁴C ages) (Menounos et al., 2013). Similarly, peat bog basal ages at sites close to the
469 present day Cordillera Darwin Ice Field suggest that ice retreated to the northern flank of Cordillera
470 Darwin between '17,009 cal. yr BP' (Punta Marinelli, Fig. 1B) and '16,356 cal. yr BP' (Punta
471 Esperanza, Fig. 1B) (Hall et al., 2013). Marine sediment core data from Seno Almirantazgo (core
472 NBP0505_JPC77) show a transition from ice-proximal facies to ice-distal facies occurred in two steps,
473 'the first at ~ 15.5 ka and the second at ~ 12.5 ka' marking the 'retreat of Marinelli Glacier from the
474 Seno Almirantazgo' (Boyd et al., 2008), with 'marine fjord' conditions established by '9800 cal. yr BP'
475 (Bertrand et al., 2017) (Marine Sediment core NBP0505_JPC67). Basal dates of macrofossils from
476 organic infills on the southern flank of the present-day Cordillera Darwin Ice Field include '12,097 cal
477 yr BP' (Caleta Olla, CO-07-02), '14,768 cal yr BP' ('Ventisquero Holanda, H-07-01) and '10,485' and
478 '14,486 cal yr BP' (Bahía Pía, BL-07-15 and BL-07-16B; locations in Fig. 1B) (Hall et al., 2013).

479
480 Overall, the geochronological evidence suggests, either different behaviors of the Cordillera Darwin
481 Ice Lobes ('early retreat' vs. 'late glacial advance hypothesis'), or that many of the regional
482 radiocarbon dates are not close minimum ages for ice retreat. The latter interpretation is consistent
483 with the generally late onset of peat deposition at subantarctic latitudes (see Table 1 in Hodgson et
484 al., 2014) which may be related to improving climatic conditions favouring plant growth and the
485 preservation of datable material rather than being close minimum ages for ice retreat. This followed
486 the cold and dry conditions resulting from increased Southern Hemisphere sea ice and northward
487 displacement of the westerlies. We therefore cannot rule out that the ice advance occurred during
488 the LGM (MIS2) or earlier. The onset of woody peat accumulation (Unit II) overlying the diamicton
489 (Unit I) at Cabo West at 12,880 cal. yr BP may therefore not be a close minimum age for the ice
490 advance along Paso Mantellero.

491

492

493 4.3 Establishment of Magellanic moorland and subpolar trees (12,880–8650 cal. yr BP)

494 The deposition of woody peat from 12,880 (10,640) – 8650 cal. yr BP suggest that woody Magellanic
495 moorland plants such as *Empetrum rubrum* and *Nothofagus* were established on the west coast of
496 Isla Hermite. This overlaps with studies showing an early Holocene expansion of *Nothofagus* forests
497 in the Magellan region in response to warmer and more humid climatic conditions after ‘c. 10,750–
498 9700’ cal. yr BP (McCulloch et al., 2020). It coincided with (and followed) the early Holocene climate
499 optimum (1.3 ± 0.3 °C warmer than present) in the James Ross Island ice core off the northern end of
500 the Antarctic Peninsula from c. 12.5 to 9.2 ka (Mulvaney et al., 2012; Fig. 1A). The establishment of
501 woody Magellanic moorland plants on the extreme west coast of Isla Hermite is notable because it
502 may imply a (weakening or) southward shift of the SHW during the Southern Hemisphere early
503 Holocene climate optimum. This behavior, whereby the SHW shift Southwards during Holocene
504 warm periods, is consistent with SHW records from southwestern Patagonia between 51°S and 53°S
505 (Moreno et al., 2021), records from the last millennium (Perren et al., 2020) and current period of
506 warming (Deng et al., 2022). At present, and since 8010 cal. yr BP, the stronger winds and associated
507 sea spray, appear to have prevented woody peat from accumulating on immediately inland of the
508 coastal cliffs. The small pockets of *Nothofagus* present today are mainly restricted to protected
509 north and south facing coastal valleys and the lee side of some of the larger hills. However woody
510 moorland plants such as *Empetrum rubrum* are more widespread and grow to within a few 100 m of
511 the coast (Supplementary Fig. 3B), so this interpretation needs to be replicated elsewhere in the
512 Islas Hermite and Islas Wollaston.

513

514 4.4 Local erosional or aeolian deposition (8650–8010 cal. yr BP).

515 The abrupt end of woody peat accumulation (Unit II) was marked by the onset of a short c. 640-year
516 period of layered grey-brown sands and silt deposition (Unit III). This consisted of a 102 cm thick
517 layer at Cabo West (Fig. 4C) and a much thinner ~3 cm thick layer at Punta Momberg (Fig. 5B).
518 Immediately inland, sediment cores from the three sites that span the early Holocene (HER24L, 44L,
519 and 49L; Fig. 3) did not include this unit, showing continuous peat accumulation across this interval.
520 This implies that Unit III is restricted to the coast, is spatially uneven in thickness, and is therefore
521 likely related to local erosional or aeolian processes on the island or in Paso Mantellero. Potential
522 local processes include the mobilization of wind-blown material from a nearby coastal blowout;
523 these occur along much of the west coast of Isla Hermite (Fig. 3). It could also be the result of
524 enhanced coastal erosion resulting from the rapid ~10–14 m relative sea level rise at ‘8500–6500’

525 cal. yr BP, inferred from dated marine terraces at eastern and western Isla Navarino respectively,
526 reaching levels of ~8 m and > 10 m above present (Björck et al., 2021).

527

528 Whilst we attribute Unit III to local erosional or aeolian processes, it coincides with a climate shift to
529 drier conditions and forest contraction recorded in a number of southern Patagonian records. This
530 included a period of ‘intense dryness between c. 9700 – 7050 cal. a BP’ from the pollen preservation
531 evidence at Punta Burslem (McCulloch et al., 2020), which may in part explain the loss of woody
532 shrubs and trees and the lack of peat accumulation on Isla Hermite at this time. Further analyses of
533 the inland peat and lake deposits will determine if this regional climate shift extended as far as Isla
534 Hermite.

535

536 4.5 Holocene peat accumulation (8010 cal. yr BP to present)

537 The Unit IV woody Magellanic subpolar forest peat that characterised this specific coastal site on Isla
538 Hermite during the early Holocene climate optimum (Unit II) did not become re-established during
539 the Holocene. Instead, the coastal sites accumulated a mossy organic peat from 8010 cal. yr BP to
540 the present. The onset of peat accumulation in the coastal sections coincides with a ‘brief return to
541 relatively wetter conditions at c. 8300 cal. a BP’ at Punta Burslem and a gradual, but latitudinally
542 variable, increase in SHW activity in Patagonia (McCulloch et al., 2020). The sustained peat
543 accumulation at Isla Hermite from 15,400 cal. yr BP at the near coastal sites (HER14L, Figs. 3B and
544 6C), and from 8010 cal. yr BP to present in the coastal sections implies westerly storm tracks and
545 associated precipitation were sufficient to maintain peat accumulation through the Late Glacial and
546 Holocene.

547

548

549 **5. Conclusions**

550

551 This paper contributes to understanding the extent and volume of the Patagonian Ice Sheet during
552 the LGM and its subsequent deglaciation. Glacial tills deposited on the west coast of Isla Hermite
553 suggest an ice lobe extended south from Cordillera Darwin down Paso Mantellero and past Isla
554 Hermite. This was similar in extent, but larger than, the Canal Beagle and Lago Fagnano Ice Lobes
555 which extended to the east. It supports the interpretation that LGM ice extended past the Cape Horn
556 archipelago, as first suggested by Nordenskjöld in 1899, and more recently inferred with ‘low
557 confidence’ by Davies et al. (2020; Fig. 33). The onset of woody peat accumulation (Unit I, Unit II
558 transition) provides a minimum age for retreat of the ice lobe of 12,880 cal. yr BP. Analyses of

559 further terrestrial deposits and marine sediment cores are recommended to further constrain the
560 glaciation history of this ice lobe including identifying landforms and bedforms associated with ice
561 streaming, and lift off due to postglacial relative sea level rise (cf. Bertrand et al., 2017; Björck et al.,
562 2021). The woody peat accumulation from 12880 cal. yr BP suggests a southward shift of the SHW
563 occurred during the early Holocene climate optimum. This was followed by a brief period of local
564 aeolian deposition and Holocene and Late Glacial peat accumulation from 8010 cal. yr BP on the
565 coast and 15,400 cal. yr BP inland.

566

567

568 **Acknowledgements**

569 Fieldwork was planned and facilitated by colleagues at Instituto Antártico Chileno (INACH) including
570 José Retamales (Director), Dr Marcelo Leppe (Head of Scientific Department), Javier S. Arata
571 (Collaborating scientist) Félix Bartsch, Wendy Rubio, Antonio Supanar (Head of Logistics and Science
572 support), Universidad de Magallanes (J-C A, EI) and Ashly Fusiarski (BAS). Armada de Chile is thanked
573 for field input by the Captain and crews of Chilean icebreaker Almirante Óscar Viel and uplift by the
574 Coastguard vessel CNS Alacalufe. DAH, SJR and BBP were supported by NERC grant NE K004515 1. EI
575 was supported by Fondecyt 1130381. J-CA was supported by Fondecyt 1130381 and ANID/BASAL
576 FB210018. FDV was supported by a CNRS INSU-ARTMIS grant for the AMS ^{14}C performed at the
577 LMC14 Laboratory in Saclay, Paris. RMCC was supported by ANID R20F0002 (PATSER) and Fondecyt
578 1200727. Laura Gerrish (BAS) provided mapping expertise for Figs. 1 and 2. Steve Colwell (BAS),
579 Paola Uribe Raibaudi (Dirección Meteorológica de Chile) and Felipe Rifo Esposito (Jefe Centro
580 Meteorológico Marítimo Región de Magallanes y Antártica Chilena, Armada de Chile) are thanked
581 for meteorological data from Cape Horn. The research was carried out under permits from
582 Corporación Nacional Forestal Región de Magallanes y Antártica Chilena (334/2014) and Ministerio
583 de Relaciones Exteriores Dirección de Fronteras y Límites del Estado (320/2014).

584

585

586 **Author contributions**

587 DAH and SJR wrote the grant supporting the work. DAH, SJR, EI and BP carried out the fieldwork
588 which was coordinated by J-CA. SJR calibrated the radiocarbon dates and stratigraphic analyses and
589 SJR, SJD and TB carried out MSCL and ITRAX analyses with FDV providing the density correction and
590 LMC14 radiocarbon dates. All authors contributed to the writing.

591

592

593 **Data availability statement**

594 The original contributions presented in the study are included in the article/Supplementary Material,
595 further inquiries can be directed to the corresponding author. Data has been deposited in the NERC
596 EDS UK Polar Data Centre (PDC)) at <https://doi.org/>.... Data and code are available on [Github](#).

597

598

599 **References**

- 600 Armada-de-Chile, 2000. Islas Wollaston y Hermite [material cartográfico] por el Servicio Hidrográfico
601 y Oceanográfico de la Armada de Chile, Mapoteca. Disponible en Biblioteca Nacional Digital de Chile
602 <http://www.bibliotecanacionaldigital.gob.cl/bnd/631/w3-article-331699.html> . Accedido en
603 22/04/2022.
- 604 Belokopytov, I.E., Beresnevich, V.V., 1955. Giktorf's peat borers. Torfyanaya Promyshlennost 8, 9–10.
- 605 Bentley, M., Sugden, D., Hulton, N.R.J., McCulloch, R., 2005. The landforms and pattern of
606 deglaciation in the Strait of Magellan and Bahía Inútil, southernmost South America. Geografiska
607 Annaler: Series A, Physical Geography 87, 313-333.
- 608 Bertrand, S., Lange, C.B., Pantoja, S., Hughen, K., Van Tornhout, E., Wellner, J.S., 2017. Postglacial
609 fluctuations of Cordillera Darwin glaciers (southernmost Patagonia) reconstructed from
610 Almirantazgo fjord sediments. Quaternary Science Reviews 177, 265-275.
- 611 Bishop, T., 2021. Itrax Data Analysis Tools Version 1.4. URL <https://thomasbishop.uk>.
- 612 Björck, S., Lambeck, K., Möller, P., Waldmann, N., Bennike, O., Jiang, H., Li, D., Sandgren, P., Nielsen,
613 A.B., Porter, C.T., 2021. Relative sea level changes and glacio-isostatic modelling in the Beagle
614 Channel, Tierra del Fuego, Chile: Glacial and tectonic implications. Quaternary Science Reviews 251,
615 106657.
- 616 Blaauw, M., Christen, J.A., 2011. Flexible paleoclimate age-depth models using an autoregressive
617 gamma process. 457-474.
- 618 Boyd, B.L., Anderson, J.B., Wellner, J.S., Fernández, R.A., 2008. The sedimentary record of glacial
619 retreat, Marinelli Fjord, Patagonia: Regional correlations and climate ties. Marine Geology 255, 165-
620 178.
- 621 Boyle, J.F., Chiverrell, R.C., Schillereff, D., 2015. Approaches to Water Content Correction and
622 Calibration for µXRF Core Scanning: Comparing X-ray Scattering with Simple Regression of Elemental
623 Concentrations, in: Croudace, I.W., Rothwell, R.G. (Eds.), Micro-XRF Studies of Sediment Cores:
624 Applications of a non-destructive tool for the environmental sciences. Springer Netherlands,
625 Dordrecht, pp. 373-390.
- 626 Bronk Ramsey, C., 2016. OxCal v. 4.4. <https://c14.arch.ox.ac.uk/oxcal.html>.

- 627 Caldenius, C., 1932. Las glaciaciones cuaternarias de la Patagonia y Tierra del Fuego. Geografiska
628 Annaler 14, 1-164.
- 629 Coronato, A., Martínez, M.A., Rabassa, J., 2004. Glaciations in Argentine Patagonia, southern South
630 America, in: Ehlers, J., Gibbard, P.L. (Eds.), Quaternary Glaciations - Extent and Chronology, Part III.
631 Elsevier, pp. 49-67.
- 632 Coronato, A., Salemme, M., Rabassa, J., 1999. Palaeoenvironmental conditions during th early
633 peopling of Southernmost South America (Late Glacial-Early Holocene, 14-8 ka B.P.). Quaternary
634 International 53/54, 77-92.
- 635 Coronato, A., Seppälä, M., Ponce, J.F., Rabassa, J., 2009. Glacial geomorphology of the Pleistocene
636 Lake Fagnano ice lobe, Tierra del Fuego, southern South America. Geomorphology 112, 67-81.
- 637 Darvill, C.M., Bentley, M.J., Stokes, C.R., Hein, A.S., Rodés, Á., 2015. Extensive MIS 3 glaciation in
638 southernmost Patagonia revealed by cosmogenic nuclide dating of outwash sediments. Earth and
639 Planetary Science Letters 429, 157-169.
- 640 Davies, B.J., Darvill, C.M., Lovell, H., Bendle, J.M., Dowdeswell, J.A., Fabel, D., García, J.-L., Geiger, A.,
641 Glasser, N.F., Gheorghiu, D.M., Harrison, S., Hein, A.S., Kaplan, M.R., Martin, J.R.V., Mendelova, M.,
642 Palmer, A., Pelto, M., Rodés, Á., Sagredo, E.A., Smedley, R.K., Smellie, J.L., Thorndycraft, V.R., 2020.
643 The evolution of the Patagonian Ice Sheet from 35 ka to the present day (PATICE). Earth-Science
644 Reviews 204, 103152.
- 645 Davies, S.J., Lamb, H.F., Roberts, S.J., 2015. Micro-XRF scanning applications in palaeolimnology -
646 recent developments, in: IW, C., RG, R. (Eds.), Micro-XRF Studies of Sediment Cores, Developments
647 in Palaeoenvironmental Research series,. Springer.
- 648 Deng, K., Azorin-Molina, C., Yang, S., Hu, C., Zhang, G., Minola, L., Chen, D., 2022. Changes of
649 Southern Hemisphere westerlies in the future warming climate. Atmospheric Research 270.
- 650 Dussaillant, I., Berthier, E., Brun, F., Masiokas, M., Hugonnet, R., Favier, V., Rabatel, A., Pitte, P., Ruiz,
651 L., 2019. Two decades of glacier mass loss along the Andes. Nature Geoscience 12, 802-808.
- 652 García, J.L., Kaplan, M.R., Hall, B.L., Schaefer, J.M., Vega, R.M., Schwartz, R., Finkel, R., 2012. Glacier
653 expansion in Southern Patagonia throughout the antarctic cold reversal. Geology 40, 859-862.
- 654 Glasser, N., Jansson, K., 2008. The Glacial Map of southern South America. Journal of Maps 4, 175-
655 196.
- 656 Guilderson, T.P., Burckle, L., Hemming, S., Peltier, W.R., 2000. Late Pleistocene sea level variations
657 derived from the Argentine Shelf. Geochemistry, Geophysics, Geosystems 1.
- 658 Gunn, D.E., Best, A.I., 1998. A new automated nondestructive system for high resolution multi-
659 sensor core logging of open sediment cores. Geo-Marine Letters 18, 70-77.

- 660 Hall, B.L., Porter, C.T., Denton, G.H., Lowell, T.V., Bromley, G.R.M., 2013. Extensive recession of
661 Cordillera Darwin glaciers in southernmost South America during Heinrich Stadial 1. Quaternary
662 Science Reviews 62, 49-55.
- 663 Hodgson, D.A., Graham, A.G.C., Roberts, S.J., Bentley, M.J., Ó Cofaigh, C., Verleyen, E., Vyverman,
664 W., Jomelli, V., Favier, V., Brunstein, D., Verfaillie, D., Colhoun, E.A., Saunders, K., Selkirk, P.M.,
665 Mackintosh, A., Hedding, D.W., Nel, W., Hall, K., McGlone, M.S., Van der Putten, N., Dickens, W.A.,
666 Smith, J.A., 2014. Terrestrial and submarine evidence for the extent and timing of the Last Glacial
667 Maximum and the onset of deglaciation on the maritime-Antarctic and sub-Antarctic islands.
668 Quaternary Science Reviews 100, 137-158.
- 669 Hogg, A.G., Heaton, T.J., Hua, Q., Palmer, J.G., Turney, C.S.M., Souton, J., Bayliss, A., Blackwell, P.G.,
670 Boswijk, G., Bronk Ramsey, C., Pearson, C., Petchey, F., Reimer, P., Reimer, R., Wacker, L., 2020.
671 SHCal20 Southern Hemisphere Calibration, 0–55,000 Years cal BP. Radiocarbon 62, 759-778.
- 672 Hugonet, R., McNabb, R., Berthier, E., Menounos, B., Nuth, C., Girod, L., Farinotti, D., Huss, M.,
673 Dussaillant, I., Brun, F., Kääb, A., 2021. Accelerated global glacier mass loss in the early twenty-first
674 century. Nature 592, 726-731.
- 675 Hulton, N.R.J., Purves, R.S., McCulloch, R.D., Sugden, D.E., Bentley, M.J., 2002. The Last Glacial
676 Maximum and deglaciation in southern South America. Quaternary Science Reviews 21, 233-241.
- 677 Lamy, F., Kaiser, J., Ninnemann, U., Hebbeln, D., Arz, H.W., Stoner, J., 2004. Antarctic Timing of
678 Surface Water Changes off Chile and Patagonian Ice Sheet Response. Science 304, 1959 - 1962.
- 679 McCulloch, R.D., Bentley, M.J., Tipping, R.M., Clapperton, C.M., 2005a. Evidence for late-glacial ice
680 dammed lakes in the central Strait of Magellan and Bahía Inútil, southernmost South America.
681 Geografiska Annaler 87 A, 335-362.
- 682 McCulloch, R.D., Blaikie, J., Jacob, B., Mansilla, C.A., Morello, F., De Pol-Holz, R., San Román, M.,
683 Tisdall, E., Torres, J., 2020. Late glacial and Holocene climate variability, southernmost Patagonia.
684 Quaternary Science Reviews 229, 106131.
- 685 McCulloch, R.D., Fogwill, C.J., Sugden, D.E., Bentley, M.J., Kubik, P.W., 2005b. Chronology of the last
686 glaciation in central strait of magellan and bahía inútil, southernmost south america. Geografiska
687 Annaler: Series A, Physical Geography 87, 289-312.
- 688 Menounos, B., Clague, J.J., Osborn, G., Davis, P.T., Ponce, F., Goehring, B., Maurer, M., Rabassa, J.,
689 Coronato, A., Marr, R., 2013. Latest Pleistocene and Holocene glacier fluctuations in southernmost
690 Tierra del Fuego, Argentina. Quaternary Science Reviews 77, 70-79.
- 691 Moreno, P.I., Henríquez, W.I., Pesce, O.H., Henríquez, C.A., Fletcher, M.S., Garreaud, R.D., Villa-
692 Martínez, R.P., 2021. An early Holocene westerly minimum in the southern mid-latitudes.
693 Quaternary Science Reviews 251, 106730.

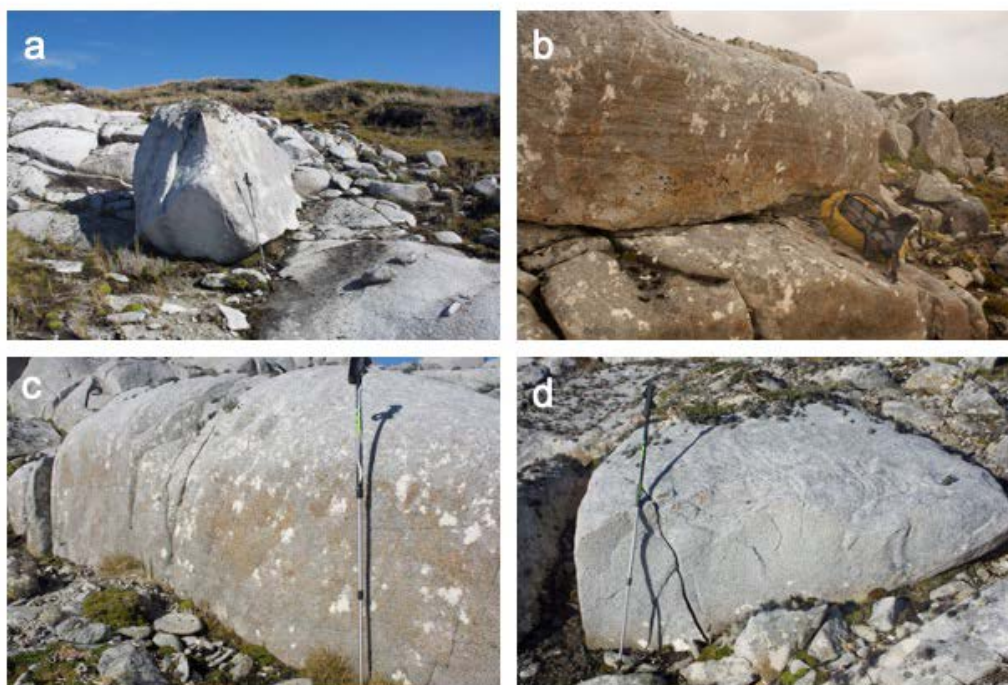
- 694 Mulvaney, R., Abram, N.J., Hindmarsh, R.C.A., Arrowsmith, C., Fleet, L., Triest, J., Sime, L.C., Alemany,
695 O., Foord, S., 2012. Recent Antarctic Peninsula warming relative to Holocene climate and ice-shelf
696 history. *Nature* 489, 141-144.
- 697 Nordenskjöld, O., 1899. Geologie, Geographie und Anthropologie. Schwedischen Expedition nach den
698 Magellansländern, 1895-1897. Norstedt & Söner, Stockholm.
- 699 Peltier, C., Kaplan, M.R., Birkel, S.D., Soteres, R.L., Sagredo, E.A., Aravena, J.C., Araos, J., Moreno, P.I.,
700 Schwartz, R., Schaefer, J.M., 2021. The large MIS 4 and long MIS 2 glacier maxima on the southern
701 tip of South America. *Quaternary Science Reviews* 262, 106858.
- 702 Perren, B.B., Hodgson, D.A., Roberts, S.J., Sime, L., Van Nieuwenhuyze, W., Verleyen, E., Vyverman,
703 W., 2020. Southward migration of the Southern Hemisphere westerly winds corresponds with
704 warming climate over centennial timescales. *Communications Earth & Environment* 1, 58.
- 705 Rabassa, J., Coronato, A., Martinez, O., 2011. Late Cenozoic glaciations in Patagonia and Tierra del
706 Fuego: an updated review. *Biological Journal of the Linnean Society* 103, 316-335.
- 707 Roberts, S.J., Monien, P., Foster, L.C., Loftfield, J., Hocking, E.P., Schnetger, B., Pearson, E.J., Juggins,
708 S., Fretwell, P., Ireland, L., Ochyra, R., Haworth, A.R., Allen, C.S., Moreton, S., Davies, S.J., Brumsack,
709 H.-J., Bentley, M.J., Hodgson, D.A., 2017. Past penguin colony responses to explosive volcanism on
710 the Antarctic Peninsula. *Nature Communications* doi:10.1038/ncomms14914.
- 711 Sandoval, F., De Pascale, G., 2020. Slip rates along the narrow Magallanes Fault System, Tierra Del
712 Fuego Region, Patagonia. *Scientific Reports* 10, 8180.
- 713 Smith, R.E., Smith, V.C., Fontijn, K., Gebhardt, A.C., Wastegård, S., Zolitschka, B., Ohlendorf, C., Stern,
714 C., Mayr, C., 2019. Refining the Late Quaternary tephrochronology for southern South America using
715 the Laguna Potrok Aike sedimentary record. *Quaternary Science Reviews* 218, 137-156.
- 716 Stern, C., Moreno, P., Henríquez, W., Villa-Martínez, R., Sagredo, E., Aravena, J., de Pol-Holz, R.,
717 2016. Holocene tephrochronology around Cochrane ($\sim 47^\circ$ S), southern Chile. *Andean Geology* 43, 1-
718 19.
- 719 Sugden, D.E., Bentley, M.J., Fogwill, C.J., Hulton, N.R.J., McCulloch, R.D., Purves, R.S., 2005. Late-
720 glacial glacier events in southernmost South America: A blend of 'northern' and 'southern'
721 hemispheric climatic signals. *Geografiska Annaler: Series A, Physical Geography* 87, 273–288.
- 722 Torres Carbonell, P.J., Guzmán, C., Yagupsky, D., Dimieri, L.V., 2016. Tectonic models for the
723 Patagonian orogenic curve (southernmost Andes): An appraisal based on analog experiments from
724 the Fuegian thrust-fold belt. *Tectonophysics* 671, 76-94.
- 725 Vanneste, H., De Vleeschouwer, F., Martinez-Cortizas, A., von Scheffer, C., Piotrowska, N., Coronato,
726 A., Le Roux, G., 2015. Late-glacial elevated dust deposition linked to westerly wind shifts in southern
727 South America. *Nature Scientific Reports* 5, 11670, doi:10.1038/srep11670.

728 Waldmann, N., Ariztegui, D., Anselmetti, F.S., Coronato, A., Austin, J.A., 2010. Geophysical evidence
729 of multiple glacier advances in Lago Fagnano (54°S), southernmost Patagonia. Quaternary Science
730 Reviews 29, 1188-1200.

731 Yan, Q., Wei, T., Zhang, Z., 2022. Modeling the climate sensitivity of Patagonian glaciers and their
732 responses to climatic change during the global last glacial maximum. Quaternary Science Reviews
733 288, 107582.

734

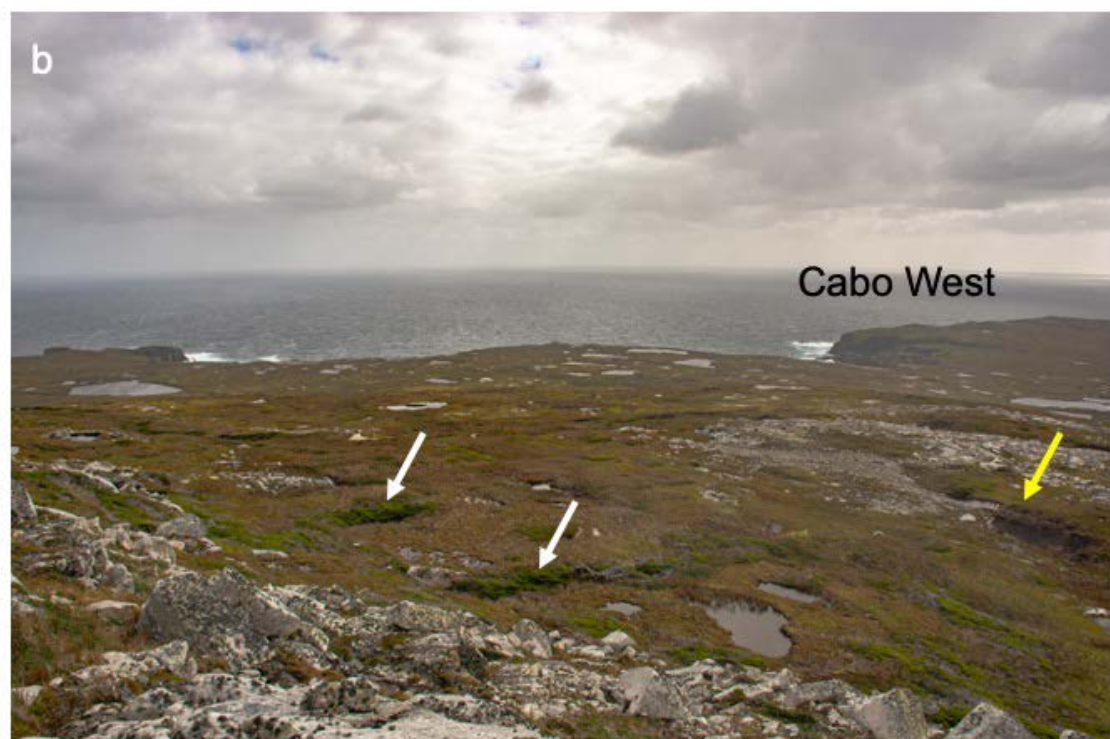
735 **Supplementary Figures**



736

737

738 S Fig. 1. Examples of striated rock surfaces and transported boulders. a) Bedrock boulder at
739 55°50.930' S, 067°52.831' W, 159 m asl. b) Striated bedrock surface. c) Vertical and horizontal
740 striations likely associated with weaknesses in the rock. D) Etching of boulder surface likely from salt
741 weathering.



742

743 S. Fig 2. A) Peat overlying boulder-strewn bedrock on Isla Hermite with white arrow showing an
744 exposure of woody peat. B) Isolated pockets of *Nothofagus antarctica* and *Empetrum rubrum* (white
745 arrows) form woody peat (yellow arrow) inland of Cabo West.

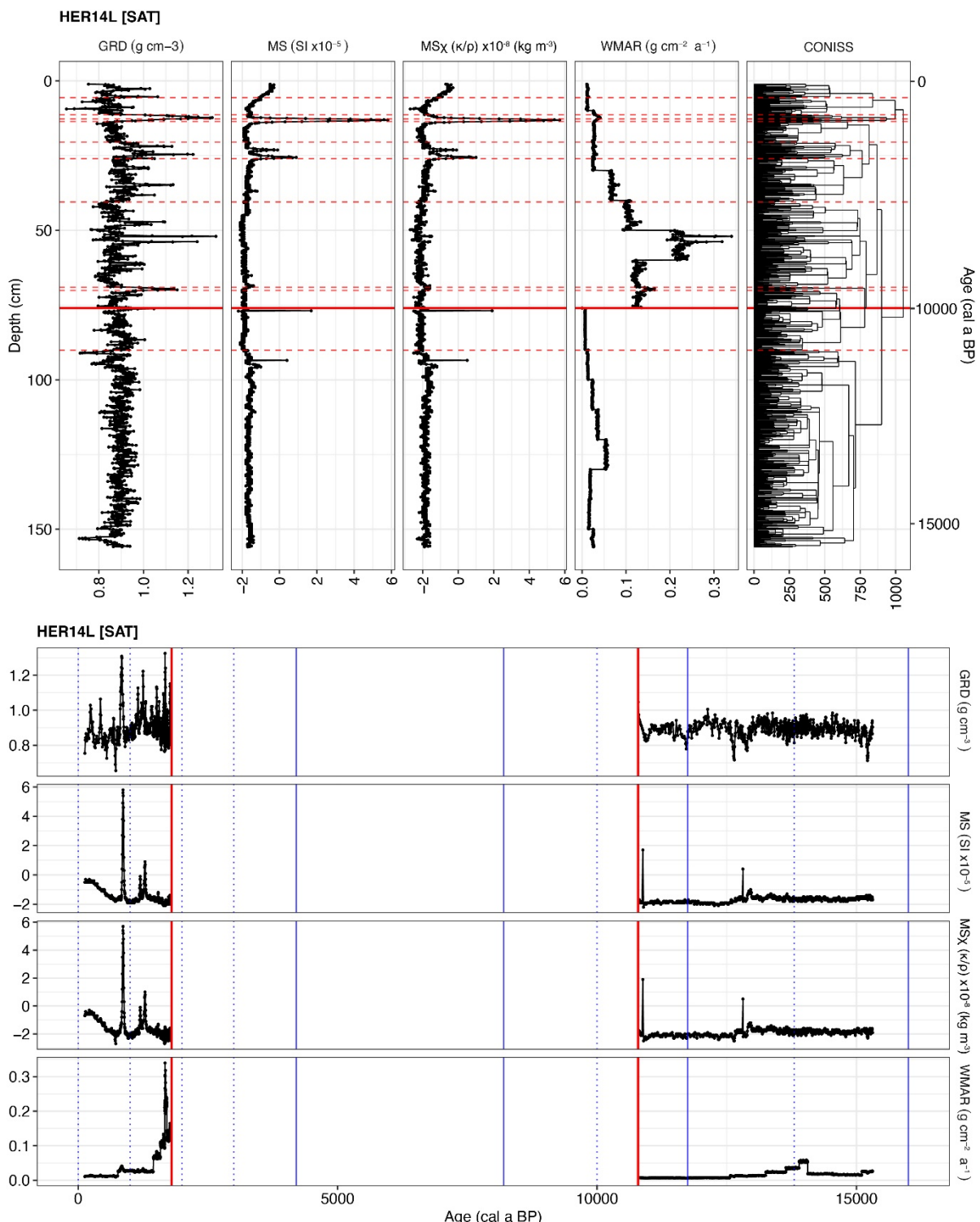
746

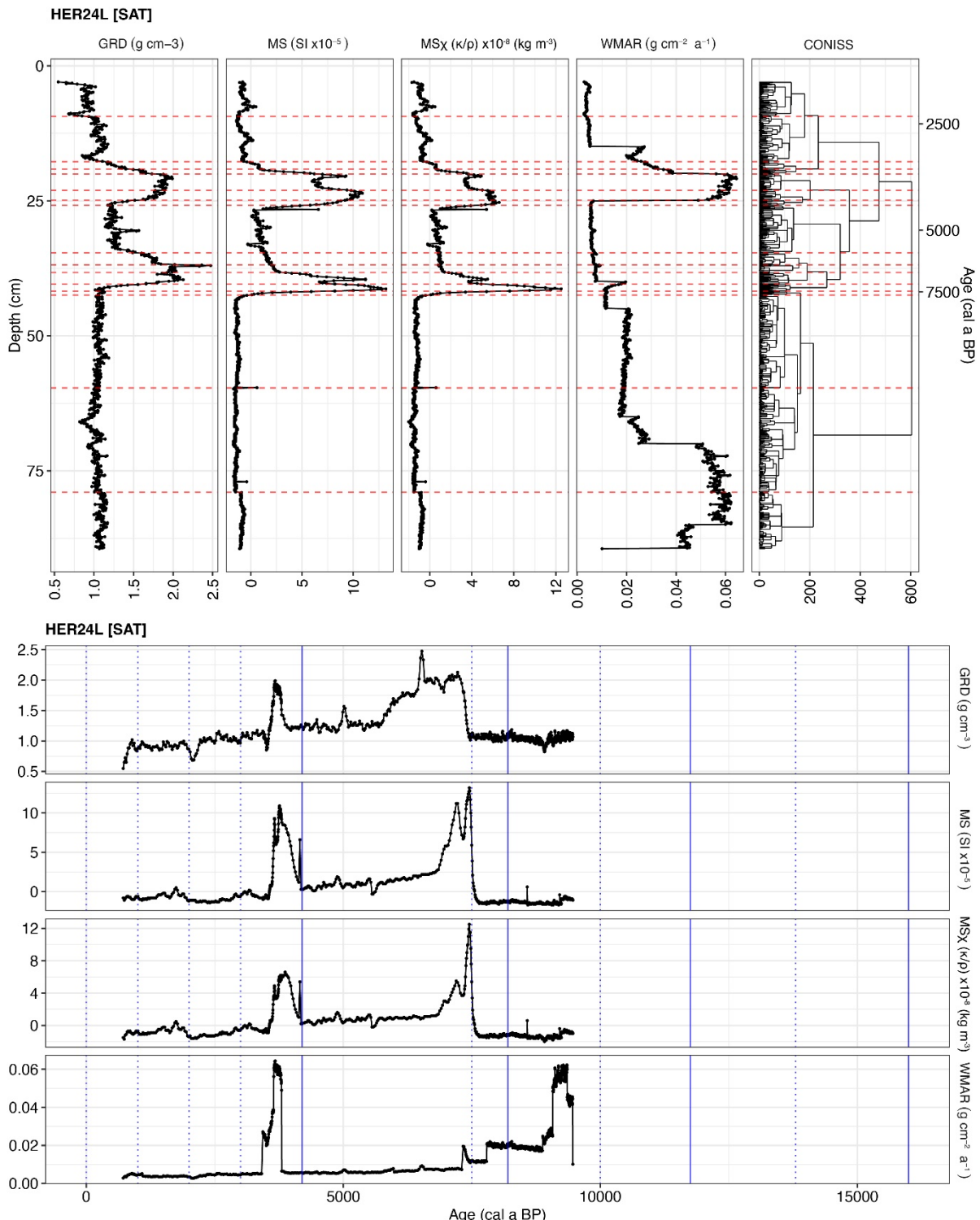


747

748 S. Fig. 3. West coast of Isla Hermite and Paso Mantellero with snow covered peaks of Isla Hoste, c.
749 80 km to the northwest.

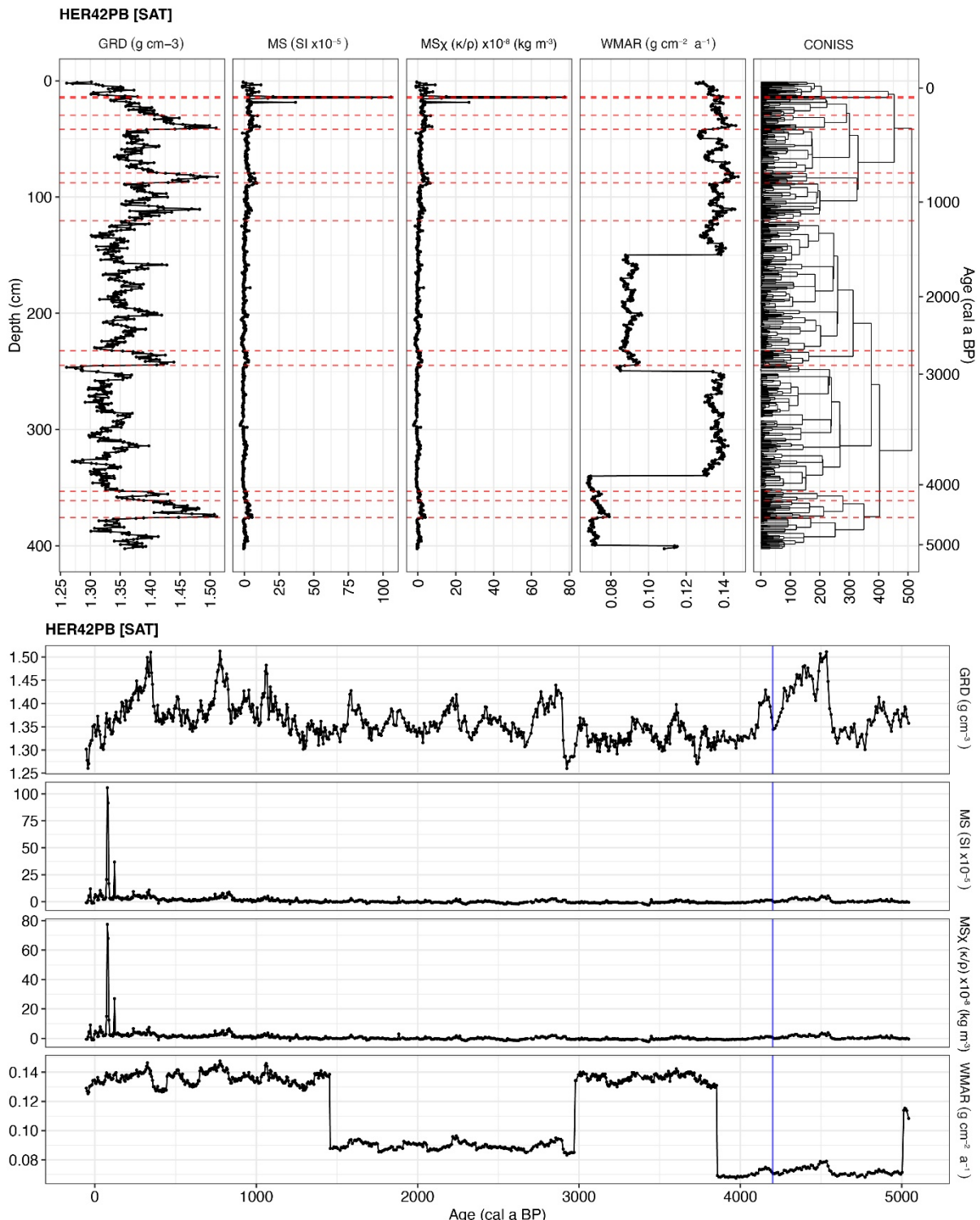
750





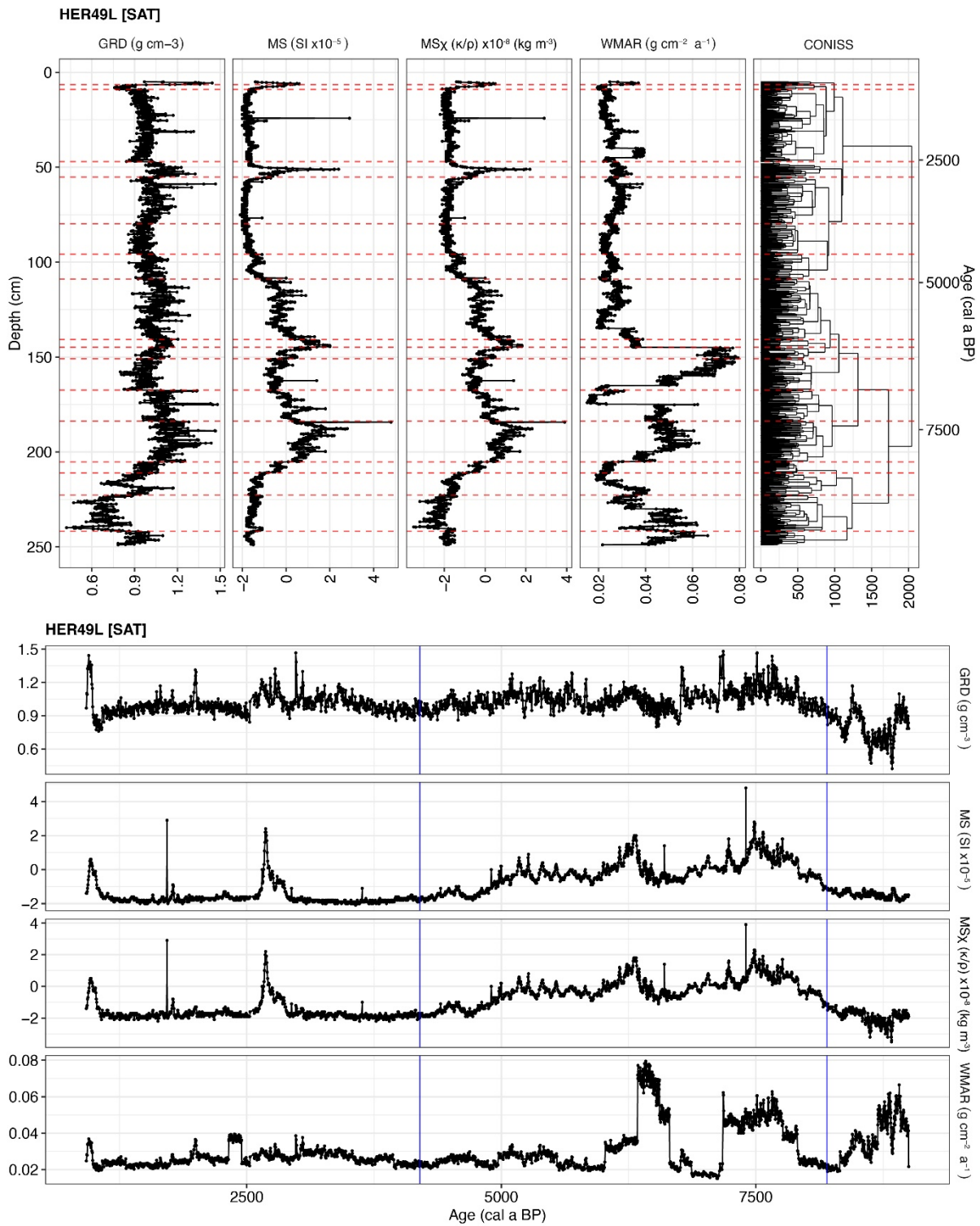
753
754

Figure S5. Summary MSCL data for HER24L, plotted against depth and age.



755
756

Figure S6. Summary MSCL data for HER42PB, plotted against depth and age.



757
758

Figure S7. Summary MSCL data for HER49L, plotted against depth and age.

Declaration of interests

The authors declare that they have no known competing financial interests or personal relationships that could have appeared to influence the work reported in this paper.

The authors declare the following financial interests/personal relationships which may be considered as potential competing interests:

